https://doi.org/10.5194/egusphere-2026-2983
Preprint. Discussion started: 12 June 2026

Evaluating Transport Observations of the Atlantic Meridional Overturning Circulation at 11°S Using an Ocean Model

Anna Christina Hans[1], Rebecca Hummels[1], Peter Brandt[1,2], Franziska U. Schwarzkopf[1], and Stephan Juricke[1,2]

[1]GEOMAR Helmholtz Centre for Ocean Research Kiel, Kiel, Germany,
[2]Faculty of Mathematics and Natural Sciences, Kiel University, Kiel, Germany

Correspondence: Anna Christina Hans (ahans@geomar.de)

Abstract. The impact of the Atlantic Meridional Overturning Circulation (AMOC) on weather and climate, both regionally and globally, motivated the installation of several observational arrays. It is vital to not only derive transport time series from these arrays but to also quantify the associated uncertainties. Here, an observing system simulation experiment is performed to assess the uncertainty and potential of the TRACOS (Tropical Atlantic Circulation and Overturning at 11°S) array to calculate the geostrophic AMOC transport ($AMOC_g$) from it. Accordingly, the observational setup is subsampled in a high-resolution ocean model and various approaches to derive $AMOC_g$ are tested. We find that the currently used approach based on bottom pressure recorders (BPRs) can explain 56 % of the short-term (seasonal to interannual) $AMOC_g$ variability, though overestimating the seasonal amplitude. Observations of longer-term variability are limited due to the pressure sensor drift. Currently, long-term (decadal to multi-decadal) variability is only captured by boundary current measurements which explain 62 % of the basin-wide $AMOC_g$ long-term variability, though with high root mean squared errors. Regarding potential improvements of the current approaches, we find: 1) The nominal drift rates of the reference sensors currently installed in self-calibrating BPRs are still too high to reliably detect a linear $AMOC_g$ trend of the magnitude presently considered realistic, namely about 1 Sv per decade. 2) Acoustic round-trip travel times are limited in use for $AMOC_g$ computation at 11°S. 3) Combining BPRs with moored temperature and salinity measurements is a promising approach that can improve $AMOC_g$ estimates of both short-term variability (to 79 % explained) and long-term variability (to 61 % explained). Overall, we find that, despite its relatively sparse instrumentation, the TRACOS array is capable of capturing AMOC signals, while we also highlight areas where uncertainties could be reduced.

1 Introduction

The Atlantic Meridional Overturning Circulation (AMOC) is a large-scale oceanic circulation that connects tropical to subpolar regions. It redistributes large amounts of physical (heat, freshwater) and biogeochemical (carbon dioxide, oxygen, nutrients) properties across all latitudes (Buckley and Marshall, 2016) and has an enormous impact on both regional weather and

https://doi.org/10.5194/egusphere-2026-2983
Preprint. Discussion started: 12 June 2026

global climate (Collins et al., 2019). These impacts motivated ongoing efforts to monitor the variability and long-term changes of the AMOC. In particular, multiple long-term observational arrays are in place, such as OSNAP (Overturning in the Subpolar North Atlantic Program) between 52°N and 60°N, RAPID-MOCHA (Rapid Climate Change - Meridional Overturning Circulation and Heat-flux Array) at 26.5°N, MOVE (Meridional Overturning Experiment) at 16°N, TRACOS (Tropical Atlantic Circulation and Overturning at 11°S) at 11°S, and SAMBA (South Atlantic Meridional Overturning Circulation Basin-wide Array) at 34.5°S (for an overview see Frajka-Williams et al., 2019, and references therein).

In addition to obtaining time series of the AMOC volume transport, it is important to properly evaluate the uncertainties associated with the individual AMOC estimates from the different arrays (Frajka-Williams et al., 2023; Foukal et al., 2026). Evaluating uncertainties is crucial to assess how reliable the calculated AMOC transports are and how the AMOC observations could be improved, which is an ongoing effort (McCarthy et al., 2020). Uncertainties result from both measurement uncertainty (related to the accuracy and drifts of sensors) and methodological uncertainty. Methodological uncertainty arises from the sensitivity of the AMOC volume transport estimates to the sampling characteristics, utilised methodological choices, and assumptions (Frajka-Williams et al., 2023). For example, it has been shown for the SAMBA array that the use of different data sets (Argo data versus a mooring array), which come with differences in the AMOC computation, can result in distinct differences in the derived AMOC variability (Chidichimo et al., 2023). The array design and methodologies for AMOC computation vary further between the arrays, partly due to historical reasons or geographical features (Frajka-Williams et al., 2019). These variations not only complicate the comparison of AMOC estimates between the arrays but also the comparison with and validation of ocean and climate models (Frajka-Williams et al., 2023).

Methodological uncertainty can be evaluated using an observing system simulation experiment (OSSE). In an OSSE, observing systems are mimicked in a model and compared with the full-field solution (hereinafter referred to as model truth). When interpreting OSSE results, it should be kept in mind that model-specific biases potentially lead to over- or underestimation of the influence of observing system components and methodological choices (Frajka-Williams et al., 2023). Several OSSEs have already been performed to assess the suitability of observational arrays for AMOC estimates. Those experiments focus mainly on the RAPID array (Hirschi et al., 2003; Baehr et al., 2004; Stepanov et al., 2016; Sinha et al., 2018; Danabasoglu et al., 2021). Others have also been performed for the SAMBA array (Perez et al., 2011), the OSNAP array (Li et al., 2017), and the MOVE array (Danabasoglu et al., 2021), whereby the focus of the studies varies between the actual array design with varying degrees of idealisation and the choice of latitude for the array placement. Deviations of the simulated array-reconstructed AMOC transport from the model-true AMOC transport arise mainly from: 1) the reference level bias (A reference level is required, for example, when using the thermal wind equation. It is typically determined as either a level of no motion or a level of known motion), 2) unsampled regions, and 3) neglected ageostrophic transport, as listed in Sinha et al. (2018). These deviations reflect also the main problems identified by the other studies mentioned above. Despite existing deviations, the OSSEs of the RAPID and OSNAP arrays show good agreement between the array-simulated and model-true AMOC. The RAPID array is expected to capture the AMOC variability to high accuracy as the standard deviation of the bias is one order smaller than the

https://doi.org/10.5194/egusphere-2026-2983
Preprint. Discussion started: 12 June 2026

standard deviation of the transport itself (Sinha et al., 2018). The OSNAP array is expected to reproduce the AMOC well as the array-simulated and model-true AMOC time series correlate with coefficients of 0.89 (0.87) for OSNAP West (East) and the root-mean-square difference is smaller than (similar to) the standard deviation of the model-true AMOC (Li et al., 2017).

So far, there are two OSSEs for AMOC estimates in the South Atlantic, including results close to or at 11°S. Baehr et al. (2009) test the suitability of applying the RAPID monitoring strategy at multiple latitudes in the South Atlantic, assuming moorings with perfect vertical coverage. They find the highest correlation between the simulated array-reconstructed AMOC and model-true AMOC (0.83 for present day climate and 0.91 for a climate change scenario) at 11°S. The time-mean AMOC transport is reconstructed best further south, which the authors associate with reduced non-geostrophic density fluctuations away from the equator and with a larger Coriolis parameter. Perez et al. (2011) test the skill to observe the AMOC by simulating both an idealised dynamic height mooring array and a an array of current and pressure recording inverted echo sounders (CPIES, where IES stands for inverted echo sounder, the C indicates the equipment with a current meter, and the P indicates the equipment with a pressure sensor which is equivalent to a bottom pressure recorder (BPR)). They find that, similar to Baehr et al. (2009), the simulated mooring array accurately reproduces the model-true AMOC, with a correlation of about 0.95 at 15°S. However, the simulated CPIES array has skill only at higher latitudes. At 15°S, a quite small dynamic height anomaly range leads to a correlation between the model-true AMOC and the simulated CPIES-reconstructed AMOC of only 0.5.

This study aims to assess how reliably the TRACOS array at 11°S can be used to compute the AMOC transport at different time scales. Since 2013, the TRACOS array has been in place, consisting of moorings and PIES. The velocity measurements of the mooring array, including an earlier mooring period from 2000-2004, have been used to study boundary currents, namely the North Brazil Undercurrent and the Deep Western Boundary Current (Hummels et al., 2015; Schott et al., 2005) and the Angola Current (Kopte et al., 2017). The bottom pressure measurements have been used to study basin-wide seasonal AMOC variability (Herrford et al., 2021). While the model studies of Baehr et al. (2009) and Perez et al. (2011) suggest that the AMOC can be calculated using an idealised mooring array at 11°S, there has been no methodological test to date for reconstructing the AMOC transport using the TRACOS array setup. To assess and optimise the AMOC estimate at 11°S, an OSSE study was recommended by the Tropical Atlantic Observing System review report (Johns et al., 2021). Following up on this recommendation, we perform an OSSE to assess the skill of the TRACOS array for computing the AMOC, the sensitivity to the methodological assumptions used, and possible improvements. Three different approaches to compute the AMOC are considered: 1) based on the bottom pressure method as applied in Herrford et al. (2021), 2) based on a RAPID- and OSNAP-like method with moored temperature (T) and salinity (S) for the interior transport while boundary currents are measured directly, and 3) based on a SAMBA-like method utilising acoustic round-trip travel times. The performance of the AMOC reconstruction will be assessed for both short-term (seasonal to interannual) and long-term (decadal to multi-decadal) variability. The detection of long-term variability of the AMOC is particularly relevant as the AMOC is suggested to be one of the tipping elements in the changing climate system (Collins et al., 2019). The short-term variability of the AMOC transport is also of interest, especially as it is tightly linked to the meridional heat transport variability (Dong et al., 2021; Johns et al., 2023; Garzoli et al., 2013). With that,

https://doi.org/10.5194/egusphere-2026-2983
Preprint. Discussion started: 12 June 2026

the AMOC variability at 11°S is linked to tropical variability in general (e.g., by the linkage to the subtropical cell (Tuchen et al., 2020)). Further, discrepancies in the seasonal representation of the AMOC in models and observations (Perez et al., 2011; Dong et al., 2014; Herrford et al., 2021; Lozier et al., 2019) might point to model biases and highlight the importance of exploring the potential of an AMOC array to not only capture long-term but also short-term variability.

The study is organised as follows: The TRACOS array and the ocean model in which the array is subsampled are described in sections 2.2 and 2.1, respectively. The computation of the AMOC volume transport is described in general in section 2.3 and in more detail for application to the TRACOS array in section 2.4. The statistics used to evaluate the array-reconstruction are described in section 2.5. The results for subsampling the observational strategies from the model output are presented in section 3, separately for the utilisation of bottom pressure data (section 3.1), moored temperature and salinity data (section 3.2), and acoustic round-trip travel time data (section 3.3). The different strategies are then combined in section 3.4 to identify improvements in the computation of the AMOC from the TRACOS array. The findings on the performance of the current approach and possible improvements are then discussed in section 4.

2 Data and Methods

2.1 Ocean model configuration VIKING20X

At the locations of the TRACOS array observations, the output fields of a high-resolution ocean-only simulation based on the VIKING20X model configuration are subsampled. Based on the NEMO code version 3.6 (Madec et al., 2017), employing the two way nesting technique provided by AGRIF (Debreu et al., 2008), VIKING20X consists of a grid at 1/20° horizontal resolution covering the Atlantic Ocean, embedded in a global grid at 1/4° horizontal resolution. In the vertical, the grid has 46 z-levels of which 25 are spread in the upper 1200 m. The bathymetry in the high-resolution region of VIKING20X is interpolated from ETOPO2 (NOAA National Geophysical Data Center, 2006). Given the limited vertical resolution, at each grid point, the actual height of a bottom cell can be reduced to better fit the bathymetry (Barnier et al., 2006). There is a linearised, filtered free surface which damps fast external gravity waves while conserving ocean volume (Roullet and Madec, 2000). Here, we use the simulation VIKING20X-JRA-OMIP (Biastoch et al., 2021) which is driven by atmospheric boundary conditions provided by the JRA55-do dataset (Tsujino et al., 2018) for the period from 1958 to 2023. This study only considers model output since 1980 to avoid biases from spin-up after initialisation from rest in 1958. The model configuration as well as the specific simulation are described in more detail in Biastoch et al. (2021).

We use model output at daily averaged resolution. Geostrophic velocities are then computed from temperature and salinity and referenced to the sea surface height (SSH) gradient, and bottom pressures are computed following Eq. (5) including the SSH contribution after freshwater budget correction. As there is no pressure load from the atmosphere in the model, such a pressure load is also not included in the computation of bottom pressure. Further note that, as VIKING20X has been run using

https://doi.org/10.5194/egusphere-2026-2983
Preprint. Discussion started: 12 June 2026

the EOS80 equations of state, all following computations will be performed using EOS80 to remain consistent in the model environment. The seawater library (Morgan and Pender, 2014) was thus used for calculations in this study.

A prerequisite for an OSSE is to have a dynamically consistent ocean model which is somewhat realistic. In VIKING20X, sea surface salinity restoring is applied to prevent too strong model drift due to the lack of ocean-atmosphere feedbacks in a forced simulation. This, however, leads to artificial changes to the freshwater fluxes at the surface which, together with further, forcing immanent, imbalances in the surface freshwater fluxes, are corrected in terms of their global budget at each model time step. Doing so prevents the modelled global mean SSH, which is derived from the local divergence of the velocity field and the balance of all local surface freshwater fluxes, from drifting. Sea level changes induced by mass changes at regional scales (monometric), for example by circulation, and by mass changes at global scales (barystatic), for example by ice melting, are included in VIKING20X. Steric sea level changes induced by density variations through expansion and contraction are omitted at global scales by using the Boussinesq approximation. However, regional gradients of steric sea level are still included in the model computations (Greatbatch, 1994; Griffies and Greatbatch, 2012).

Regarding the representation of the AMOC, VIKING20X was found to be comparable to other high-resolution models in a model intercomparison review (Hirschi et al., 2020). The AMOC in VIKING20X was validated against observations by Biastoch et al. (2021). They found that, compared to AMOC observations from the RAPID array, the model simulation used in this study underestimates both monthly and interannual AMOC variability as indicated by the standard deviations. Compared to observations from the TRACOS array, the structure of the western boundary current system is represented quite well by the model, with the mean North Brazil Undercurrent and Deep Western Boundary Current transports being possibly overestimated. Further, the peak-to-peak amplitude of the seasonal cycle of the model-true AMOC at 11°S in VIKING20X is by a factor 2 smaller compared to the observational estimate from Herrford et al. (2021) for the period 2013 to 2018. These differences between observations and model could hint at two implications for the interpretation of the OSSE: First, the contribution of the boundary currents to the basin-wide transport might be overstated. Second, the contribution of seasonal variability on the total variability might be underestimated. Moreover, the AMOC in VIKING20X exhibits interannual variability and a weakening of 1.15 $\mathrm{Sv\,decade^{-1}}$ since 1994 at 11°S. An AMOC trend of -1.15 $\mathrm{Sv\,decade^{-1}}$ is in the range of CMIP6 projections until 2100 (Weijer et al., 2020) and is comparable to the RAPID trend estimate from 2004 to 2023 (McCarthy et al., 2025). Even though the existence of an AMOC trend in current observations remains under debate (Lobelle et al., 2020; Terhaar et al., 2025), it is important to assess whether the TRACOS observing system has the potential to detect such AMOC variability and trend.

2.2 TRACOS array setup

The TRACOS array, formerly also referred to as TSAA (Tropical South Atlantic Array at 11°S), is a long-term observatory (Fig. 1). It consists of four tall moorings (WB1, WB2, WB3, WB4) near the western boundary (WB) off Brazil and one tall mooring (EB1) near the eastern boundary (EB) off Angola. All moorings are equipped with MicroCATs measuring temperature

https://doi.org/10.5194/egusphere-2026-2983
Preprint. Discussion started: 12 June 2026

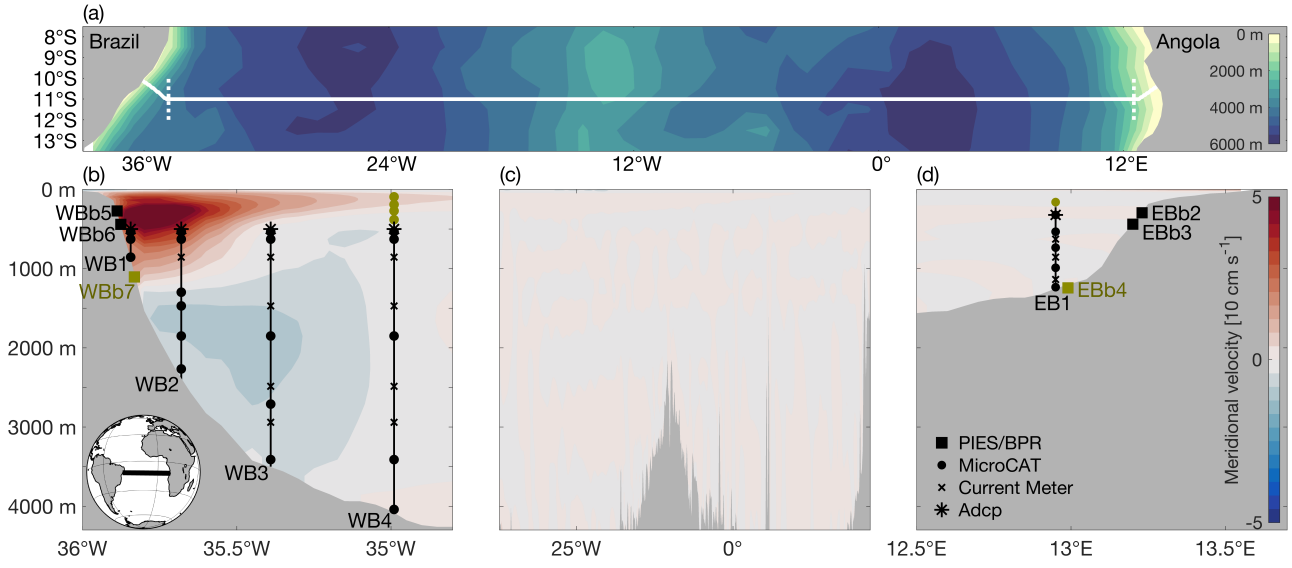

Figure 1. Overview of the simulated TRACOS observing system. (a): Geographical location of the TRACOS section (white line) on which PIES and moorings are located. The surrounding bathymetry from etopo2 is shown in colour. The vertical, dotted white lines at 34.8 °W and 12.5°E indicate the longitudinal separation for (b)-(d). (b)-(d): TRACOS section as depth versus longitude with a zoom on the western (b) and eastern (d) boundary. The initial design of the TRACOS array is indicated by the black symbols with latest additions to the current design indicated in yellowish. The time-mean meridional velocity field of VIKING20X along the TRACOS section is shown in colour. While the displayed mean meridional velocity field is tilted at the boundaries to fit the tilt of instrument positions (white line in (a)), note that the model-true AMOC in this study is integrated following a straight line along 11°S.

and conductivity (from which salinity is then derived) and with point current meters and acoustic Doppler current profilers measuring velocity. Additionally, there are two PIES at the western boundary at about 300 m and 500 m depth (WBb5, WBb6), measuring bottom pressure and acoustic round-trip travel time. At the eastern boundary, there have been two BPRs (EBb2, EBb3), roughly matching the deployment depth of the western boundary PIES. The array has been in place since 2013, although there have been a few changes in the meantime. Two changes are considered in this study (marked in yellowish in Fig. 1b+d): 1. Position of the eastern boundary bottom measurements: The two BPRs (EBb2 and EBb3) at about 300 m and 500 m depth could not be recovered more than once likely due to extensive fishing in the region. After a few years gap, they have been replaced by a PIES at 1200 m depth (EBb4). It is planned to also deploy a complementary PIES at 1200 m at the western boundary (WBb7). 2. Refining the WB4 and EB1 moorings: For the WB4 mooring, four temperature and salinity sensors were added in the upper 500 m in early 2025. For the EB1 mooring, one temperature and salinity sensor was added at 150 m depth in early 2026. In addition to the moored instruments, there are satellite measurements providing data of sea surface height, sea surface temperature, and surface wind stress. Note that sea surface salinity measurements from satellites are not accurate

https://doi.org/10.5194/egusphere-2026-2983
Preprint. Discussion started: 12 June 2026

enough yet to be used. Gridded climatologies from Argo profiles can be considered as auxiliary data sets.

Even though this study does not address measurement uncertainty, one limitation of the measurements should be noted: Bottom pressure measurements are affected by sensor drift (Watts and Kontoyiannis, 1990) with a mean drift of -0.1 $\mathrm{dbar\,year^{-1}}$ and 90 % of drifts observed in the range $\pm$ 0.8 $\mathrm{dbar\,year^{-1}}$ (Polster et al., 2009) which is rather larger than the bottom pressure variations induced by geostrophic transport variations (e.g., amplitudes of 0.1 dbar in the Atlantic at about 37°N and 11°S (Watts and Kontoyiannis, 1990; Herrford et al., 2021)). The sensor drift is not predictable but can be modelled by a combination of an exponential and a linear function of the form $a_1 \cdot (1 - e^{-a_2 \cdot x}) + a_3 \cdot x + a_4$, being accurate to at least 0.02 dbar (Watts and Kontoyiannis, 1990; Polster et al., 2009). However, this modelled drift also contains and thus removes oceanic signals related to low-frequency variability. As a consequence of the drift of the BPRs and of the levelling problem (depth of the BPRs at the eastern and western boundary are not exactly matching (Donohue et al., 2010)), only temporal anomalies of pressure and not absolute pressure values are considered in this study.

The 1/20°horizontal resolution of the used model mostly allows for precisely picking the instrument positions. The positions of the PIES at the western boundary continental shelf had to be slightly adjusted to better fit the actual deployment depth. The differences between reality and model in the depth of instruments of the TRACOS array are summarised in Table A1. Essentially, the model is subsampled at locations that are slightly shallower than those of the PIES and BPRs in the real ocean. For easier readability, I will refer in the following to PIES and BPRs at 300 m, 500 m, and 1200 m depth, even though the actual depths differ slightly from these depth levels as shown in Table A1. Whilst the positions of the instruments in the TRACOS array were picked as accurately as possible from the model, no attempt was made to identify actual positions for satellite data; instead, these were simply assumed to be given at each model grid point. While the TRACOS array is nominally at 11°S, the instrument locations actually vary between 10.94°S and 10.23°S as the western and eastern boundary sections are aligned perpendicular to the coast. Due to the tilt, the number of moorings and space in between moorings capturing the boundary currents is minimised.

Note that no observational data from the TRACOS array have been used in this study. For the OSSEs, pseudo-observations are taken from the model output and then used for the AMOC calculations.

2.3 Calculating AMOC volume transport

At a specified latitude, the AMOC volume transport is defined as the maximum of the overturning stream function Ψ:

$$AMOC(t) \approx \max_z \Psi(z,t) = \max_z \int_z^0 \int_{WB}^{EB} v(x,z',t)\,dx\,dz' = \int_{z_m}^0 \int_{WB}^{EB} v(x,z,t)\,dx\,dz \tag{1}$$

https://doi.org/10.5194/egusphere-2026-2983
Preprint. Discussion started: 12 June 2026

where v is the meridional velocity and z_m the depth of maximum overturning. The temporal mean of z_m is 1100 m (Fig. 2d) and corresponds to the boundary between northward flowing Antarctic Intermediate Water and southward flowing upper North Atlantic Deep Water. Here, the AMOC is computed in depth space which should resemble a computation in density space as isobars and isopycnals align well at lower latitudes.

Typically, the AMOC transport is approximated by the sum of the geostrophic AMOC transport ($AMOC_g$) and the Ekman transport, with the latter being calculated from the wind stress:

$$AMOC(t) = AMOC_g(t) + Ekman(t) = \int_{z_m}^{0} \underbrace{\int_{WB}^{EB} v_g(x,z,t)\,dx}_{T_g(z,t)}\,dz - \int_{WB}^{EB} \frac{\tau_{x,wind}(x,t)}{\rho_{0,surface}\cdot f}\,dx \tag{2}$$

where v_g is the geostrophic meridional velocity, T_g the meridional geostrophic transport at depth z across the basin, $\tau_{x,wind}$ the zonal wind stress, $\rho_{0,surface} = 1024.2\ \mathrm{kg\,m^{-3}}$ the mean model density at the surface across the 11°S section, and f the Coriolis parameter. Geostrophic motion results from the equilibrium between the pressure gradient force and the Coriolis force. Hence, T_g can be computed as:

$$T_g(z,t) = \int_{WB}^{EB} v_g(x,z,t)\,dx = \frac{1}{\rho_0 \cdot f} \cdot \Big(p_{EB}(z,t) - p_{WB}(z,t)\Big) \tag{3}$$

where p is the pressure and $\rho_0 = 1025\ \mathrm{kg\,m^{-3}}$ the reference density (as used in VIKING20X). Applying the hydrostatic equation, it follows for the surface:

$$T_g(z=0,t) = \frac{g}{f} \cdot \Big(SSH_{EB}(t) - SSH_{WB}(t)\Big) \tag{4}$$

where g is the gravitational acceleration and SSH sea surface height.

Additionally, the thermal wind equation can be used, which relates the vertical shear of geostrophic velocities and the horizontal density gradient. Combining the geostrophic balance and the thermal wind relation, p can also be calculated from density (ρ) measurements with p being referenced to the surface:

$$p(z,t) = g \cdot \int_{z}^{0} \rho(z',t)\,dz' + g \cdot \rho(z=0,t) \cdot SSH(t) \tag{5}$$

To ensure that the geostrophic balance is valid at 11°S, the corresponding transport is calculated with monthly averaged data. 11°S is the target latitude chosen for f and g. The AMOC at 11°S is considered the model truth.

2.4 Deriving geostrophic AMOC transport from the TRACOS array

The procedure to compute $AMOC_g$ from the TRACOS array varies depending on the data set used. Currently, the $AMOC_g$ transport at 11°S is calculated based on bottom pressure measurements. However, the TRACOS array also includes moored

https://doi.org/10.5194/egusphere-2026-2983
Preprint. Discussion started: 12 June 2026

temperature and salinity data and acoustic round-trip travel time data, which could also enable the computation of the geostrophic transport. The options for using bottom pressure, moored temperature and salinity, and acoustic round-trip travel time measurements will be presented individually.

2.4.1 Using bottom pressure

When the pressure at both sides of the basin is known, T_g can be directly calculated from Eq. (3). This applies for the TRACOS array at roughly 300 m and 500 m depth and has already been applied by Herrford et al. (2021). They determined T_g at two more depth levels (surface and z_m). Applying Eq. (4) gives T_g at the surface. Introducing a level of no net motion across the basin gives $T_g = 0$ at the mean depth of maximum overturning, which is at 1100 m depth in the employed model. To obtain $AMOC_g$ from vertical integration according to Eq. (2), the vertical structure between the four depth levels with known T_g is set either by interpolation (associated identifier for methodological overview Table 1: b-vst #3 and #4) or by regression onto Empirical Orthogonal Functions (EOFs, b-vst #1 and #2) with the new vertical grid having a regular resolution of 10 m. The EOFs are computed from the model-true T_g which is (unless otherwise stated) referenced to the level of no net motion. Regressed onto the depth levels with known T_g are the first two (unless otherwise stated) EOFs, which explain 76 % and 19 % of the variance, respectively. When using a level of no net motion, this level automatically corresponds to the lower bound of integration z_m in Eq. (2). Note that even for the case of utilising a level of known motion (b-vst #2 or b-stp #4 or #5), integration is performed until 1100 m. As only temporal anomalies of pressure can be considered (see section 2.2), only transport anomalies can be determined (T_g' and $AMOC_g'$), not the time-mean transport. Hence, the level of no net motion also becomes a level of only no net variability. Note that with SSH chosen at the coasts, this method provides full basin $AMOC_g'$ without missing any transport towards the topography.

There are two limitations to the method as described in Herrford et al. (2021). The bottom pressure data are subject to sensor drift (b-prc) and there are data gaps at the eastern boundary (b-ebb). These two limitations are simulated in this study, considering current handling (b-prc #1 and b-ebb #1) as well as some alternatives. Further, sensitivity tests of the method and associated assumptions are performed considering the depth of the level of no net motion (b-ref), the approximation of the vertical structure (b-vst), and modifications to the instrumental setup (b-stp), as summarised in Table 1.

2.4.2 Using moored temperature and salinity

Moored temperature and salinity measurements can be used to calculate pressure, following Eq. (5), from which the geostrophic transport between two moorings can be calculated using Eq. (3). This strategy is used for the interior geostrophic transport of the RAPID array (McCarthy et al., 2015) and the interior geostrophic transports of the OSNAP array (Lozier et al., 2019), though employing dynamic height instead of pressure as an intermediate variable. The boundary current transports are directly inferred from boundary current measurements. As at 11°S direct velocity measurements of the western and eastern boundary

https://doi.org/10.5194/egusphere-2026-2983
Preprint. Discussion started: 12 June 2026

Table 1. List of methodological choices tested for the $AMOC'_g$ reconstruction based on bottom pressure data. This table also serves as a legend for Tables 3, 4, 5, 7, and B1.

b-prc	**Approach for pressure sensor drift**
#0	Original model values (no drift)
#1	De-drifting every 2.3 years (roughly corresponding to the average deployment length)
#2	High-pass filtering with 2 year cut-off
#3	Original model values + low drift (mimicking self-calibrating A-0-A (ambient-zero-ambient) BPRs) with linear drifts of (a) $2 \cdot 10^{-3}$ dbar year^{-1}, (b) $1 \cdot 10^{-3}$ dbar year^{-1}, (c) $7 \cdot 10^{-5}$ dbar year^{-1}, or (d) $1 \cdot 10^{-5}$ dbar year^{-1}
#4	De-drifting every 2.3 years; WB: adding yearly BP values reconstructed from IES
#5	EB: de-drifting every 2.3 years; WB: reconstruction from WB4 mooring following Eq. (9) using WB4 mooring with (a) current setup (m-wb4 #2), or (b) enhanced setup (m-wb4 #3)
b-ebb	**Approach for eastern boundary BPRs**
#0	Original model values
#1	Annual & semi-annual harmonics of model BP values from the first two years (1980-1981)
#2	Reconstruction from EB1 mooring (m-eb1 #1) and EBb4 BPR following Eq. (8)
#3	Like #2 but with the EB1 mooring contribution high-pass filtered with 2 years cut-off
b-ref	**Depth level assumed as level of no net motion**
#1	1100 m
#2	900 m
#3	1300 m
b-vst	**Method to approximate vertical structure**
#1	EOF (referenced to level of no net motion) regression
#2	EOF (referenced to surface geostrophic transport) regression
#3	Linear interpolation
#4	Spline interpolation
#5	Above 500 m: EOF regression; below 500 m: linear interpolation
b-stp	**Depth levels for which T_g is derived from BPRs**
#1	300 m and 500 m
#2	500 m
#3	300 m
#4	300 m, 500 m and 1200 m
#5	500 m and 1200 m

exist (Hummels et al., 2015; Kopte et al., 2017), we aim here to follow up on the RAPID and OSNAP approach and reconstruct the interior part of the $AMOC_g$ transport between the moorings WB4 and EB1 based on moored temperature and salinity measurements.

https://doi.org/10.5194/egusphere-2026-2983
Preprint. Discussion started: 12 June 2026

Simulated are four different vertical setups of the moorings WB4 and EB1: an idealised setup assuming temperature and salinity measurements for each vertical model bin (associated identifier for methodological overview Table 2: m-wb4 #0 & m-eb1 #0), an initial setup that has been in place until January 2025 for the western and until February 2026 for the eastern boundary (m-wb4 #1 & m-eb1 #1), the current setup that corresponds to the latest changes (m-wb4 #2 & m-eb1 #2), and an enhanced setup that is fulfilling the recommendations for vertical spacing of the RAPID array by McCarthy et al. (2015) of having a separation of less than 100 m in the upper 500 m where density variability is strongest and separations of about 200 m between 200 m and 2000 m (m-wb4 #3 & m-eb1 #3). Note that neither the initial nor the current setup comply with these recommendations, as the moorings were designed as current meter moorings and not intended to be used as dynamic height moorings. To be able to interpolate the temperature and salinity measurements vertically (Eq. (5), the measurements are transferred on a higher-resolution vertical grid with a regular spacing of 10 m. Hence, assumptions need to be made to approximate the vertical structure (m-vst). We test two strategies that have been applied to the RAPID moored measurements - stepwise integration of temperature and salinity using monthly climatological gradients (Fillenbaum et al., 1997; Johns et al., 2005; McCarthy et al., 2015) (m-vst #1), and linear interpolation of temperature and salinity anomalies relative to climatological profiles (Williams et al., 2015) (m-vst #2) - as well as EOF regression (m-vst #3). For the 'stepwise integration' approach (m-vst #1), climatological temperature and salinity profiles for each month of the year are averaged over the model period for the moorings WB4 and EB1 considering all vertical model bins. Subsequently, vertical gradients are computed for the climatological temperature and salinity profiles, yielding $\frac{dT}{dp}$ and $\frac{dS}{dp}$ as functions of pressure (Fig. C1). These gradients are linearly interpolated onto a 1 dbar regular grid. Then, temperature and salinity profiles can be reconstructed on a 10 m grid by stepwise integrating weighted climatological gradients upwards and downwards from adjacent measurement levels:

$$T(p) = \sum_{i=1}^{2} \left(1 - \frac{|p - p_i|}{p_2 - p_1}\right) \cdot \left(T(p_i) + \int_{p_i}^{p} \frac{dT}{dp}(p')dp'\right) \tag{6}$$

where i = 1,2 are the adjacent measurement levels. The same procedure is conducted for salinity. Note that contrary to earlier applications of this method, gradients are mapped on pressure and not on temperature. For the 'linear interpolation of anomalies' approach (m-vst #2), temperature and salinity profiles for the moorings WB4 and EB1 are averaged separately over the model period considering all vertical model bins and spline-interpolated to refine the vertical spacing. These averaged and interpolated profiles serve as reference profiles. Subsequently, temperature and salinity anomalies at the measurement depths are calculated relative to the reference profiles and interpolated linearly to regular depth intervals. After adding the reference profiles again, density profiles are calculated. For the 'EOF regression' approach (m-vst #3), EOF patterns are computed for the full density profile and then the first one, two or three EOFs are regressed to the density values at the simulated measurement depths. The first EOF explains 70 % (92 %) of the variance, the second 21 % (6 %), and the third 5 % (1 %) for mooring WB4 (EB1). If an idealised mooring setup (m-wb4 #0 or m-eb1 #0) is considered, we fill the gaps between the model bins in the vertical by spline interpolation.

https://doi.org/10.5194/egusphere-2026-2983
Preprint. Discussion started: 12 June 2026

We initially assume that there are temperature and salinity measurements at the surface, which is realistic for temperature with satellite observations but up-to-date unrealistic for salinity where rather a monthly climatology is realistic with Argo float products and from CTD sections. Therefore, we test in addition to this idealised case (m-sur #0), three different methods for the realistic case of no surface salinity measurements (m-sur #1-#3) as further described in Appendix C.

The temperature and salinity measurements now available on a 10 m vertical grid up to the surface can be used to compute pressure following Eq. (5) and then T'_g following Eq. (3) and $AMOC_g$ following Eq. (2) with here a fixed overturning depth set to 1100 m. In this case, the integration is performed from the surface down to 1100 m (m-idr #1). Alternatively, T'_g can also be calculated relative to a level of no motion (z_{nomo}) in order to minimise the impact of the error in reconstructing the surface variability (m-idr #2). This leads to the density from the moored temperature and salinity measurements being integrated upwards:

$$T_g(z,t) = -\frac{g}{\rho_0 \cdot f} \cdot \int_{z_{nomo}}^{z} \rho_{EB}(z',t) - \rho_{WB}(z',t)\, dz' \tag{7}$$

where z_{nomo} is set to the time-mean of the overturning depth z_m at 1100 m. This approach is also used for the RAPID array, where the level of no motion is set to 4820 m (approximately the interface between northward flowing Antarctic Bottom Water and southward flowing lower North Atlantic Deep Water). However, McCarthy et al. (2015) also tested the calculation with a level of no motion at 1200 m (approximately the interface between northward flowing Antarctic Intermediate Water and southward flowing upper North Atlantic Deep Water) and got quite similar results.

The different methodological choices which are compared in this study for the described method based on temperature and salinity data are summarised in Table 2.

2.4.3 Using acoustic round-trip travel time

The acoustic round-trip travel time τ_{ies} of a sound pulse from the seafloor to the surface and back, as measured by IES, is a function of the temperature and salinity of the water column through which the sound pulse passed. While τ_{ies} can be fitted to all kinds of variables, such as originally the thermocline depth (Rossby, 1969), it is common to utilise the gravest empirical mode (GEM) technique to reconstruct density profiles from τ_{ies} (Meinen and Watts, 2000). The so-called GEM is a transfer function, specific for each IES location, relating τ_{ies} to the desired reconstruction properties (such as temperature, salinity, and density profiles) based on a two-dimensional look-up table which is created from hydrographic profiles. For the hydrographic profiles, τ_{ies} is first simulated as $\tau_{ies}(z,t) = 2 \cdot \int_z^0 \frac{1}{c(z',t)} dz'$, where c is the sound speed of the profile, and then related to the temperature, salinity, and density at each depth level. The profiles reconstructed with such a transfer function can then be used to compute the geostrophic transport between the IES locations. This approach is used for the geostrophic transport computation of the SAMBA array (Meinen et al., 2013, 2018) and has been used for parts of the NOAC (North Atlantic Changes) array

https://doi.org/10.5194/egusphere-2026-2983
Preprint. Discussion started: 12 June 2026

Table 2. List of methodological choices tested for the $AMOC_g$ reconstruction where the interior is based on moored temperature and salinity (T&S) data. This table also serves as a legend for Tables 6 and B2.

m-wb4	**Depth levels selected from WB4 mooring for T&S**
#0	Idealised setup: all model bins
#1	Initial setup: surface, 500m, 650m, 1900m
#2	Current setup: surface, 100m, 200m, 300m, 400m, 500m, 650m, 1900m
#3	Enhanced setup: surface, 50m, 100m, 200m, 300m, 400m, 500m, 650m, 850m, 1100m, 1900m
m-eb1	**Depth levels selected from EB1 mooring for T&S**
#0	Idealised setup: all model bins
#1	Initial setup: surface, 300m, 500m, 700m, 950m, 1200m
#2	Current setup: surface, 150m, 300m, 500m, 700m, 950m, 1200m
#3	Enhanced setup: surface, 20m, 100m, 200m, 300m, 400m, 500m, 700m, 950m, 1200m
#4	Idealised setup but climatological year (also of corresponding SSH)
m-vst	**Method to approximate vertical structure**
#1	Stepwise integration of T&S using monthly climatological gradients
#2	Linear interpolation of temporal anomalies of T&S
#3	EOF regression
	using the first (a) 1, (b) 2, or (c) 3 EOFs
m-sur	**Approach for sea surface salinity**
#0	Original model values
#1	Climatological year
#2	Depth-invariant temporal anomaly above uppermost instrument
#3	Seasonal varying extrapolation
m-idr	**Computation of T_g**
#1	Integration from surface following Eq. (5) and Eq. (3)
#2	Integration from level of no net motion (1100 m) following Eq. (7)
#3	Integrating Eq. (3) with p_{WB} following Eq. (5) and p_{EB} computed relative to a 1200 m BPR (b-prc #1) following Eq. (8)
#4	Like #3 but with p_{WB} computed relative to a 500 m BPR (b-prc #1) following Eq. (9)

at about 47°N (Rhein et al., 2019; Nowitzki et al., 2021).

Note that for the TRACOS array, reconstructed profiles from IESs WBb5, WBb6, and EBb4 can only cover the geostrophic transport in the upper 500 m. For the remaining part of the $AMOC_g$, other measurements have to be combined. Besides this, there are concerns that 11°S is not a suitable latitude for applying the GEM technique due to a small dynamic height anomaly range, as raised by Perez et al. (2011). Accordingly, in this study we test whether the density variability at the TRACOS IES locations can be captured by the GEM technique at all, and which additional information can be derived from τ_{ies} data to

https://doi.org/10.5194/egusphere-2026-2983
Preprint. Discussion started: 12 June 2026

possibly assist the methods described in the sections above. Hence, τ_{ies} is also fitted to the bottom pressure and the Fofonoff potential. For that, the bottom pressure is computed according to Eq. (5) (same as used for section 3.1). The Fofonoff potential χ (Fofonoff, 1962) in z-space is computed as $\chi(z,t) = \int_z^0 p(z',t)dz'$, where p is computed according to Eq. (5). The advantage of χ would be that the volume transport within the integration layer between two IES locations would directly follow from $\frac{1}{\rho_0 \cdot f} \cdot (\chi_2 - \chi_1)$, if χ_1 and χ_2 were integrated over the same depth range. It should be noted that the test in the model comes along with some idealisations: While in the real ocean, the hydrographic profiles are a collection of nearby CTD and Argo profiles, here in the model we use all profiles at the respective IES locations. The resulting ideal look-up tables have the advantage that the suitability of the GEM reconstruction itself can be disentangled from errors due to too few and/or horizontally too spread profiles generating the lookup table. We further do not employ a seasonal model for hydrographic profiles in the upper ocean in order to avoid noise from seasonal variability (Watts et al., 2001; Roessler et al., 2015), but simply consider yearly mean values, which is possible due to the presence of ideal hydrography in the model. It should also be noted that the IESs WBb5 and WBb6 are rather shallow with roughly 300 m and 500 m depth (definitely shallower than the IESs in the studies mentioned above) which can further increase uncertainty in reality due to a reduced signal-to-noise ratio.

2.5 Evaluating the performance of the array reconstruction

The performance of the $AMOC'_g$ reconstruction based on the simulated TRACOS array is evaluated by a comparison to the model-true $AMOC'_g$. This comparison focusses separately on the performance of capturing short-term and long-term variability as otherwise the performance of capturing short-term variability would dominate the statistics. We apply a first-order Butterworth high-pass filter with a 2 year cut-off to isolate variability shorter than two years. Similarly, we apply a second-order Butterworth low-pass filter with a 5 year cut-off to isolate variability longer than five years. The similarity of the array-reconstructed and model-true $AMOC'_g$ is then assessed by the root mean squared error (rmse) and the Pearson correlation coefficient (R) - after linearly de-trending and removing of a mean. For a sufficient performance, we expect the rmse to be smaller than the standard deviation of the model-true $AMOC'_g$. The statistics (rmse and R) for the full time series (after linearly de-trending) are given in appendix B. Further, the performance in reconstructing the seasonal cycle is assessed by the amplitude (maximum - minimum) and the phase (month of maximum) of a monthly climatology. The ability to capture long-term trends is assessed based on a linear trend since 1994. It is tested using t-statistics whether the difference between the array-reconstructed linear trend and the model-true linear trend is statistically significantly different from zero. However, the interpretability of the resulting linear trends as an AMOC climate change signal is limited, because the resulting trends could also be part of multi-decadal variability and because no robust trend analysis has been carried out.

3 Results for subsampling of observational strategies

The model-true AMOC time series at 11°S is calculated using all grid points along a straight line over the basin at 11°S. While both model-true $AMOC_g$ and the Ekman transport (Fig. 2a) are dominated by short-term (esp. seasonal) variability, $AMOC_g$ also exhibits decadal variability, with a change of -1.08 $\mathrm{Sv\,decade^{-1}}$ over the last 30 years. The Ekman transport

https://doi.org/10.5194/egusphere-2026-2983
Preprint. Discussion started: 12 June 2026

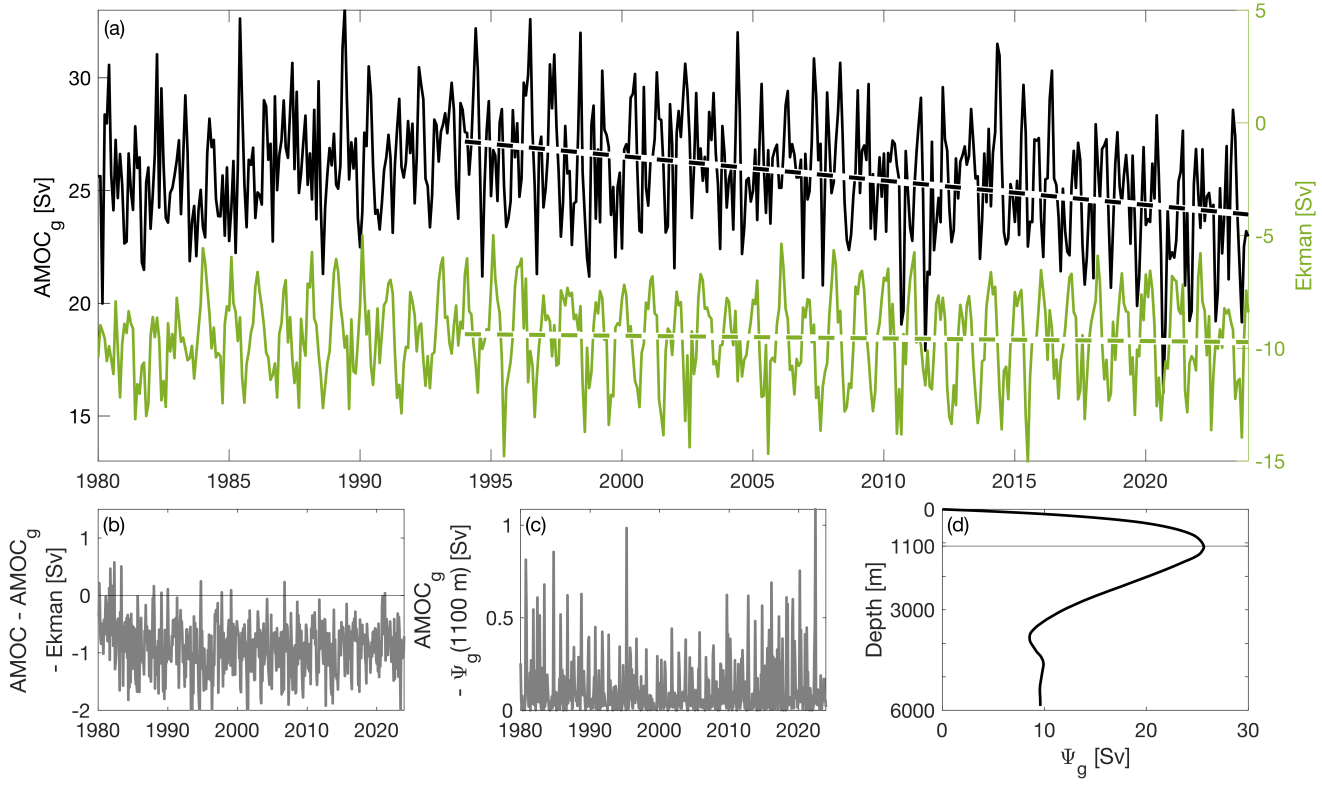

Figure 2. Overview of the model-true AMOC at 11°S in VIKING20X. (a): Model-true $\mathrm{AMOC_g}$ (black) and Ekman transport (green) time series at 11°S at monthly resolution. The y-axes of $AMOC_g$ and Ekman are only shifted relative to each other, so that the variability remains comparable. Linear trends are computed since 1994 and indicated by the dashed lines, amounting -1.08 $\mathrm{Sv\,decade^{-1}}$ for $\mathrm{AMOC_g}$ and -0.12 $\mathrm{Sv\,decade^{-1}}$ for Ekman. (b): Time series of neglected ageostrophic transport when approximating the AMOC by the sum of the geostrophic and Ekman transport (Eq. (2). (c): Time series of neglected transport when using a time-constant overturning depth z_m in Eq. (2). (d): Depth profile of the time-mean geostrophic overturning streamfunction with the horizontal line marking the maximum at 1100 m depth.

shows hardly any longer-term variability, and a linear trend over the last 30 years would only amount to -0.12 $\mathrm{Sv\,decade^{-1}}$. The approximation of the AMOC as the sum of Ekman transport and $AMOC_g$ (Fig. 2) is accurate to, on average, 0.9 Sv. The corresponding neglected ageostrophic AMOC component shows some long-term variability that originates close to where the North Brazil Undercurrent hits the topography (not shown). However, with a linear trend since 1994 of +0.05 $\mathrm{Sv\,decade^{-1}}$, the variability of the neglected ageostrophic component is much smaller and, therefore, has little effect on the long-term variability of the AMOC. Hence, other ageostrophic terms seem negligible at monthly time scales in VIKING20X, ruling out the concerns of enhanced non-geostrophic density fluctuations at 11°S as raised by Baehr et al. (2009) due to a smaller Coriolis parameter near the equator or by Perez et al. (2011) due to proximity to the equatorial wave guide. Ignoring the temporal variability of the depth of maximum overturning and integrating the geostrophic meridional transport T_g to the temporal mean depth of

https://doi.org/10.5194/egusphere-2026-2983
Preprint. Discussion started: 12 June 2026

maximum overturning at each time step (Fig. 2c) would underestimate $AMOC_g$ by, on average, 0.1 Sv. The seasonal cycle would be unaffected in phase and amplitude, and the Pearson correlation to the original $AMOC_g$ would remain at 1.00.

In the following, $AMOC_g$ will be reconstructed in VIKING20X based on the setup of the TRACOS array and then compared to the model-true $AMOC_g$.

3.1 Using bottom pressure

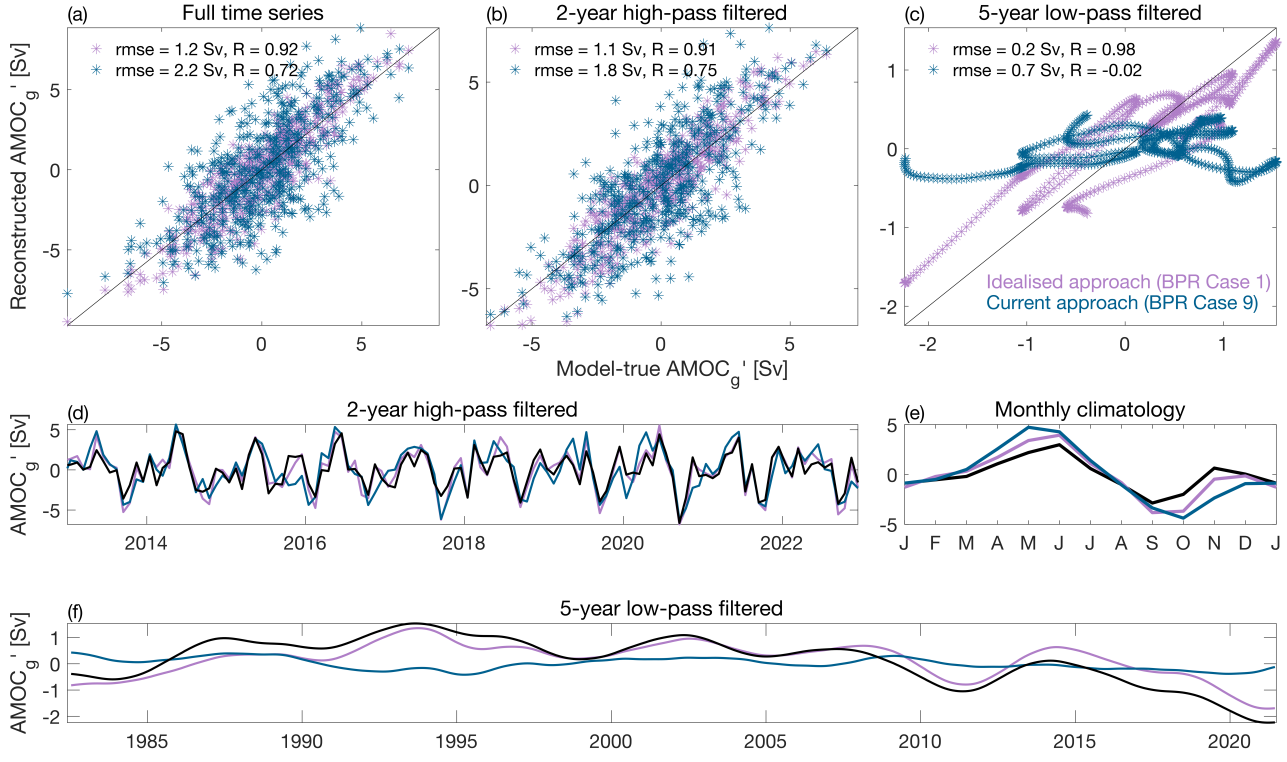

Figure 3. Comparison of $AMOC'_g$ reconstructed from BPRs with the model-true $AMOC'_g$. (a)-(c): $AMOC'_g$ reconstructed from BPRs vs. the model-true $AMOC'_g$ considering (a) the full time series, (b) the high-pass filtered time series with 2 year cut-off, and (c) the low-pass filtered time series with 5 year cut-off. The diagonal black lines indicate perfect reconstruction. Dark blue markers represent the current approach (combination of b-prc #1, b-ebb #1, b-ref #1, b-vst #1, b-stp #1, later also referred to as BPR Case 9) and light purple markers represent an idealised approach (combination of b-prc #0, b-ebb #0, b-ref #1, b-vst #1, b-stp #1, later also referred to as BPR Case 1). (d): Time series of last ten years of data in (b). The black line represents the model truth. (e): Monthly climatology of the full time series. (f): Time series of data in (c).

For the bottom pressure method, $AMOC'_g$ is computed using SSH and BPRs at about 300 m and 500 m depth at the eastern and western side of the basin as described in section 2.4.1. Assuming in a first step ideal BPRs (without sensor drift → original model bottom pressure anomalies) and no data gaps, the reconstructed $AMOC'_g$ correlates to the model-true $AMOC'_g$ with a

https://doi.org/10.5194/egusphere-2026-2983
Preprint. Discussion started: 12 June 2026

Table 3. Statistics for the simulated array-reconstruction of $AMOC'_g$ compared to the model-true $AMOC'_g$ based on the bottom pressure method with a focus on existing limitations. Computed are the root mean squared error (rmse), the Pearson correlation coefficient (R), the difference between the maximum and minimum and the month of maximum for a monthly climatology, and a linear trend for the last 30 years (i.e., since 1994). All statistics, except the trend, are computed after linearly de-trending the time series. For the model truth, the standard deviation (std) is displayed in the rmse column. A legend for the assumptions used for the presented reconstructions is given by Table 1. Case 1 and Case 9 represent the idealised (no BPR drift and no EB data gaps) and current (BPR drift and EB data gaps) approach, respectively. Colour-shading highlights how good the statistic are, the darker the better. Yellow shading relates to short-term (esp. seasonal) variability, and blue shading to long-term variability. For the linear trend, * marks that the trend of the reconstruction is not significantly different from the trend of the model truth. For the cases displayed in this table, only assumptions regarding sensor drift (b-prc) and EB data gaps (b-ebb) vary, while other parameters are unchanged (b-ref #1, b-vst #1, b-stp #1).

BPR Cases	Assumptions		High pass filtered		Monthly clim.		Low pass filtered		Linear
	b-prc	b-ebb	rmse (Sv)	R	max-min (Sv)	month of max	rmse (Sv)	R	trend (Sv decade^{-1})
model-truth			std 2.12		5.83	Jun	std 0.69		-1.08
1 ('idealised')	0	0	1.06	0.91	7.76	Jun	0.16	0.98	-0.73
Drift problem									
2	1	0	1.10	0.90	7.77	Jun	0.74	-0.05	-0.08
3	2	0	1.06	0.91	7.73	Jun	0.76	-0.19	-0.09
EB data gaps									
8	0	1	1.80	0.76	9.04	May	0.52	0.70	-1.06*
9 ('current')	1	1	1.82	0.75	9.11	May	0.73	-0.02	-0.14

Pearson correlation coefficient of 0.92 (Fig. 3 light purple). The performance of the reconstruction is good for both short and long-term variability (Fig. 3 light purple and Table 3 - Case 1). The rmse is at least a factor 2 smaller than the standard deviation of the model-true $AMOC'_g$, suggesting a sufficient signal to noise ratio for both time scales. The seasonal cycle, assessed by a monthly climatology, is well represented in terms of phase, but the amplitude is overestimated by 33 %. The linear trend of the model-true $AMOC'_g$ since 1994 of -1.08 $\mathrm{Sv\,decade^{-1}}$ is underestimated by 32 % by the reconstruction, which shows only a change of -0.73 $\mathrm{Sv\,decade^{-1}}$, with the two trends differing significantly from one another. Even if the $AMOC'_g$ reconstruction is not perfect, a method that uses only two BPRs on each side of the basin as well as SSH data and a level of no net motion is sufficient to explain $\mathrm{R}^2 = 85$ % of the $AMOC'_g$ variability at 11°S. In the following, $AMOC'_g$ will be reconstructed with taking into account the limitations of the BPR method, i.e. taking into account the drift of the BPRs and the data gaps at the eastern boundary.

https://doi.org/10.5194/egusphere-2026-2983
Preprint. Discussion started: 12 June 2026

3.1.1 Limitations due to pressure sensor drift and EB data gaps

The primary limitation of the bottom pressure method is the pressure sensor drift. Although it is not possible with an OSSE to evaluate how well the drift is explained by the combination of an exponential and a linear function, the effect of the drift removal on the removal of ocean signals can be simulated. For that, we fit for every 2.3 years (to roughly match common deployment lengths and to start at different times of the year) an exponential plus linear function after removing annual and semi-annual harmonics (following the procedure applied in Herrford et al. (2021)). Removing this fit from the simulated bottom pressure data does not affect the $AMOC'_g$ variability at time scales below 2 years which includes the seasonal cycle (Table 3 - Case 2). However, as expected, long-term variability has largely been eliminated which also includes the linear trend. Almost identical results to those obtained by removing an exponential plus linear fit are achieved when high-pass filtering the simulated bottom pressure data with a third-order Butterworth filter and a cut-off period of 2 years (Table 3 - Case 3). Hence, the removal of the pressure sensor drift does not affect $AMOC'_g$ variability with periods shorter than 2 years but it removes most of the long-term variability including the trend. Note that while the drift will always affect the long-term trend, increasing the deployment length will allow for more variability to be captured as de-drifting basically acts as a high-pass filter with the deployment length setting the cut-off period.

The second limitation of the bottom pressure method is the data gap at the EB as BPR data is only available for the first deployment period for the EB. The resulting data gap in subsequent years was filled by Herrford et al. (2021) using annual and semi-annual harmonics of the pressure measurements from the first deployment. Doing so (Table 3 - Case 8), the correlation between the reconstructed and model-true short-term $AMOC'_g$ variability decreases by 0.15, while the rmse increases by 70 % going along with a further overestimation of the seasonal cycle amplitude. The correlation and rmse between the reconstructed and model-true long-term $AMOC'_g$ variability also worsen while the linear trend gets closer to the model truth. The negative trend offset if considering the EB data gaps (hence if ignoring the long-term variability of the EB BPRs) is likely caused by ignoring the negative pressure trend at the eastern boundary, which would otherwise partially compensate the negative pressure trend at the western boundary. This effect might be reduced or even reversed in reality when also accounting for the global steric sea level rise (which is not present in VIKING20X) which would rather contribute to a positive pressure trend. An alternative interpretation of the greater similarity between the reconstructed and model-true trends in the case of neglected long-term variability of EB pressure would be that the long-term EB pressure variability contributes more noise than signal. However, the worsening in correlation and rmse in this case rather suggests that the apparent improvement in the linear trend might be merely coincidental. These results imply that neglecting the EB pressure variability worsens the $AMOC'_g$ reconstruction at short (seasonal) time scales while the impact on long-term variability is more complicated. Still, when replacing the EB pressure variability by its annual and semi-annual harmonics, 58 % (49 %) of the $AMOC'_g$ variability can still be explained for short (long) time scales when ignoring the pressure sensor drift limitation (Table 3 - Case 8).

https://doi.org/10.5194/egusphere-2026-2983
Preprint. Discussion started: 12 June 2026

Table 4. Linear trends for the simulated array-reconstruction of $AMOC'_g$ compared to the model-true $AMOC'_g$ based on the bottom pressure method when simulating self-calibrating A-0-A BPRs. Here, only the drifts added to the bottom pressure vary, while other parameters are unchanged (b-ebb #0, b-ref #1, b-vst #1, b-stp #1).

BPR Cases	Assumptions b-prc	Linear trend (Sv decade^{-1})
model-truth		-1.08
1 ('idealised')	0: no drift	-0.73
Remaining A-0-A drifts		
4	3a: $2 \cdot 10^{-3}$ dbar year^{-1}	8.81
5	3b: $1 \cdot 10^{-3}$ dbar year^{-1}	4.04
6	3c: $7 \cdot 10^{-5}$ dbar year^{-1}	-0.39
7	3d: $1 \cdot 10^{-5}$ dbar year^{-1}	-0.68

The two limitations of the bottom pressure method (pressure sensor drift and EB data gaps) lead to limited performance of the reconstructed $AMOC'_g$. With that, the currently used approach (Fig. 3 dark blue and Table 3 - Case 9), as presented in Herrford et al. (2021), explains 52 % of the model-true $AMOC'_g$, with 56 % of the short-term and 0 % of the long-term variability being captured. In section 3.4, the two limitations of the currently used BPR approach will be addressed by combining with the other data sets.

3.1.2 Potential of self-calibrating BPRs

Independent of the considerations of including other data sets to overcome the limitations of the bottom pressure method, the self-calibrating A-0-A (ambient-zero-ambient) BPR technology could make it possible to observe long-term variability of the $AMOC'_g$ with the bottom pressure method in the future. The A-0-A technology uses in addition to the ambient (standard) pressure sensor a reference sensor which is a barely drifting barometer at atmospheric pressure to which the ambient pressure sensor is regularly compared to. Doing so, the ambient pressure sensor can be calibrated, which essentially reduces the pressure drift of the ambient sensor to that of the barometer. According to the manufacturers, the drift of the currently implemented barometers is smaller than 10^{-3} dbar year^{-1} (Paroscientific barometer (Paroscientific Inc.), used by manufacturer RBR) or $2 \cdot 10^{-3}$ dbar year^{-1} (Druck barometer (Druck, 2025), used by manufacturer Sonardyne). For the Paroscientific barometer, a test of three of those barometers over a nineteen-year test period yielded a median drift rate of $7 \cdot 10^{-5}$ dbar year^{-1} (Paroscientific Inc., 2011). To test the maximum effect of the remaining drift on capturing an AMOC trend, we use the OSSE of the bottom pressure method and add the maximum and median barometer drifts. Specifically, we assume and add linear drifts -

https://doi.org/10.5194/egusphere-2026-2983
Preprint. Discussion started: 12 June 2026

Table 5. Statistics for the simulated array-reconstruction of $AMOC'_g$ compared to the model-true $AMOC'_g$ based on the bottom pressure method with a focus on the assumed vertical structure. For explanations of the statistics and shading see Table 3. A legend for the assumptions used for the presented reconstructions is given by Table 1. For the cases displayed in this table, only assumptions regarding the vertical structure (b-vst) and the setup (b-stp) vary, while other parameters are unchanged (b-prc #0, b-ebb #0, b-ref #1).

BPR Cases	Assumptions		High pass filtered		Monthly clim.		Low pass filtered		Linear
	b-vst	b-stp	rmse (Sv)	R	max-min (Sv)	month of max	rmse (Sv)	R	trend (Sv decade^{-1})
model-truth			std 2.12		5.83	Jun	std 0.69		-1.08
1 ('idealised')	1	1	1.06	0.91	7.76	Jun	0.16	0.98	-0.73
Approximate vertical structure									
12	2	1	0.98	0.92	7.20	Jun	0.16	0.97	-0.76
13	3		2.69	0.77	13.21	Jun	0.38	0.83	-0.81*
14	4		5.41	0.57	18.35	Jun	1.06	0.21	-0.90*
Reduced setup									
15	1	2	1.15	0.92	7.80	Jun	0.20	0.96	-0.89
16		3	1.21	0.88	8.01	Jun	0.21	0.95	-0.66

positive at the western and negative at the eastern boundary - to the original model bottom pressure data. The resulting linear trends of the reconstructed $AMOC'_g$ (Table 4 - Cases 4 to 6) show that the $AMOC'_g$ trend is obscured for both maximum and median barometer drifts. Hence, the currently remaining drift rates may not be sufficient to capture linear $AMOC'_g$ trends of about 1 $\mathrm{Sv\,decade^{-1}}$. A remaining drift of 10^{-5} $\mathrm{dbar\,year^{-1}}$ (Table 4 - Case 7) would be needed to be able to reconstruct the $AMOC'_g$ trend of about -1 $\mathrm{Sv\,decade^{-1}}$ with less than 10 % deviation from the no drift case. Similar conclusions can be reached when comparing the linear trend of the bottom pressure at the BPR locations (WBb5: $-3 \cdot 10^{-4}$ $\mathrm{dbar\,year^{-1}}$; WBb6: $-6 \cdot 10^{-4}$ $\mathrm{dbar\,year^{-1}}$; EBb2: $1 \cdot 10^{-5}$ $\mathrm{dbar\,year^{-1}}$; EBb3: $-3 \cdot 10^{-4}$ $\mathrm{dbar\,year^{-1}}$) to the currently remaining drift rates potentially reaching up to $2 \cdot 10^{-3}$ $\mathrm{dbar\,year^{-1}}$ as stated by the manufacturers. Note that while in reality the pressure trends might differ when accounting for global steric sea level rise, the trends of zonal pressure gradients, which are aimed to be observed, remain in the order of $3 \cdot 10^{-4}$ $\mathrm{dbar\,year^{-1}}$.

3.1.3 Sensitivity to assumed vertical structure

The sensitivity of the $AMOC'_g$ reconstruction based on the bottom pressure method is tested regarding the assumed vertical structure, i.e, regarding (1) the choice of a level of no net motion, (2) the approximation of the vertical structure, and (3) setup modifications. This is done independent of the limitations stated above, that means assuming no pressure sensor drift and no

https://doi.org/10.5194/egusphere-2026-2983
Preprint. Discussion started: 12 June 2026

EB data gaps. Hence, we test how sensitive the $AMOC'_g$ reconstruction shown in Table 5 - Case 1 is to changes regarding the vertical structure. (1) Shifting the level of no net motion by 200 m up or down (Table B1 - Cases 10 and 11) hardly impacts the statistics of the $AMOC'_g$ reconstruction. (2) Regressing EOF patterns calculated from geostrophic transports referenced to surface geostrophic transports (instead of a level of no net motion) (Table 5 - Case 12) also has little effect on the statistics of the $AMOC'_g$ reconstruction. An alternative to regressing EOF patterns to fill the vertical gaps between the instruments with a less predetermined vertical structure is vertical interpolation. However, linear interpolation (Table 5 - Case 13) strongly reduces the performance of the $AMOC'_g$ reconstruction, with the correlation between the reconstructed and model-true $AMOC'_g$ short-term (long-term) variability decreasing by 0.14 (0.15), while the rmse increases by a factor of 2.5 (2.4). Spline interpolation has also been tested but leads to even worse results (Table 5 - Case 14).

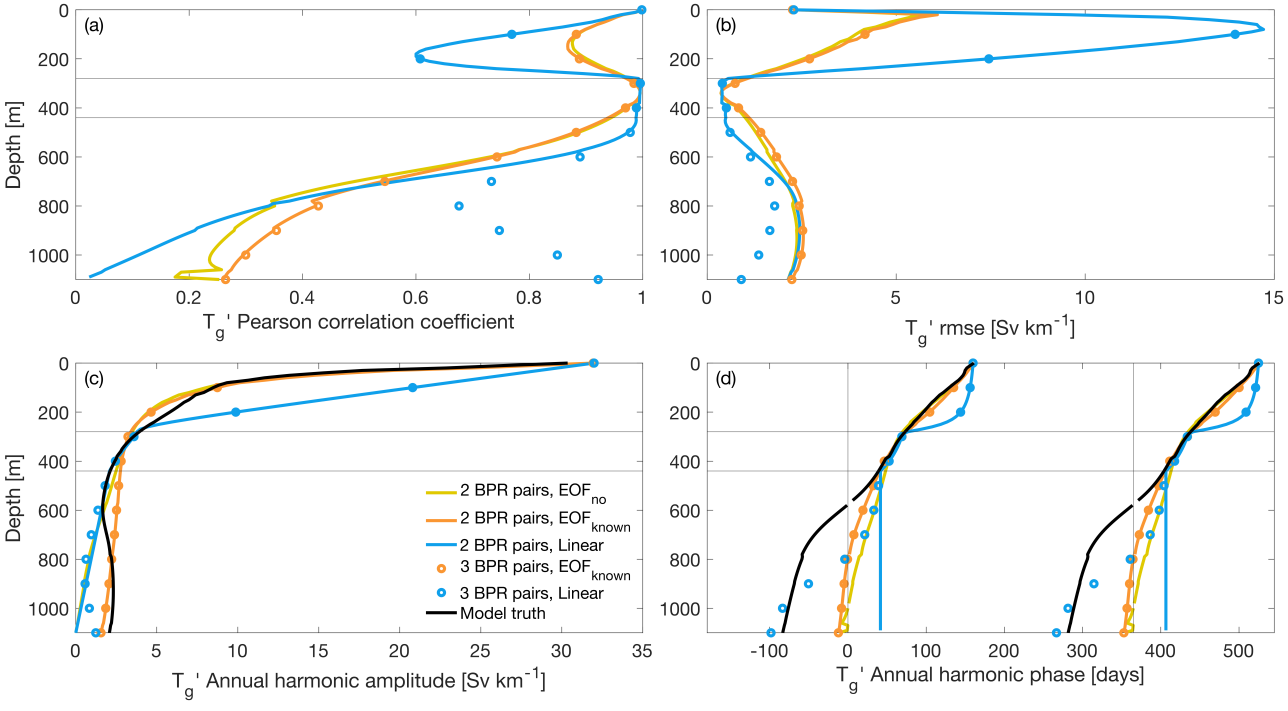

Figure 4. Statistics comparing the simulated array-reconstructed T'_g based on the bottom pressure method with the model true T'_g. The statistics used for the comparison at each depth level are (a) the Pearson correlation coefficient (R), (b) the root mean squared error (rmse), (c) the annual harmonic amplitude, and (d) the annual harmonic phase. Colours represent different assumptions regarding the vertical structure: regressing EOFs referenced to a level of no net motion (yellow, b-vst #1), regressing EOFs referenced to known surface geostrophic transport (orange, b-vst #2), and linear interpolation (blue, b-vst #3). For coloured lines, two pairs of BPRs at about 300 m and 500 m depth are considered (solid line, b-stp #1). For coloured circles, an additional BPR pair at about 1200 m depth is considered (circles, b-stp #4). For all cases, the drift problem and EB data gaps are ignored (b-prc #0, b-ebb #0). The black line represents the model truth. Grey horizontal lines mark the depth of the two simulated BPRs.

https://doi.org/10.5194/egusphere-2026-2983
Preprint. Discussion started: 12 June 2026

To actually evaluate the reconstruction of the vertical structure, we also look at T_g' (Fig. 4) and not just the depth-integrated $AMOC_g'$. T_g' reconstructed for the idealised BPR approach (Fig. 4a yellow line) shows a high correlation (R > 0.87) with the model-true T_g' in the upper 500 m. Below, the correlation decreases and reaches 0.25 at the level of no net motion. The vertical profile of the rmse (Fig. 4b yellow line) has a maximum of 5.8 $\mathrm{Sv\,km^{-1}}$ at 20 m depth and another local maximum at 930 m depth. The annual cycle (evaluated by examining annual harmonics, Fig. 4c+d yellow line) of the array-reconstruction is in phase with the one from the model truth up to the second BPR and becomes out of phase below. The annual amplitude of the array-reconstruction mainly deviates from the one from the model truth below 600 m depth. Hence, vertically, the performance is best at depths with measurements and worst towards the level of no net motion, whereby the impact of the latter is limited by the low transport variability there.

The sensitivity of the T_g' reconstruction is tested regarding (2) (approximation of vertical structure) and (3) (setup modifications). The representation of the vertical structure is similar when using EOF patterns referenced to surface geostrophic transport (Fig. 4 orange line) or referenced to a level of no net motion (Fig. 4 yellow line). Only below the depth levels with BPRs, the annual cycles differ between the two referencing options, with the referencing to surface geostrophic transport yielding an annual cycle closer to but still not equal to the model truth. These results suggest that using a structure function with a level of no net motion across the basin is justified, especially when considering that, for observations, reference velocities may contain larger errors and could therefore even degrade the reconstruction. The aforementioned alternative of linear interpolation (Fig. 4 blue line) shows overall a worse performance than EOF regression with particularly high errors between the surface and depth of the first BPR pair due to an overestimation of the annual amplitude. Although these results for the usage of linear interpolation do not appear to be promising, it should be noted that linear interpolation performs better than EOF regression at depth (below the second BPR pair at about 500 m) when an additional BPR pair is assumed at a depth of about 1200 m (Fig. 4 circles), as the EOF regression is still dominated by upper ocean variability. Thus, the T_g' reconstruction would be best when merging EOF regression until the 500 m BPR pair and linear interpolation towards the 1200 m BPR pair. However, when looking at the effect on the $AMOC_g'$ reconstruction, adding the BPR pair at 1200 m depth only slightly improves the reconstruction (Table B1 - Cases 17 to 20). Considering the setup of the BPRs, it is further interesting to note that only using one BPR pair instead of two BPR pairs hardly changes the $AMOC_g'$ reconstruction (Table 5 - Cases 15 and 16). This indicates that the bottom pressure variability signal between 300 m and 500 m depth is quite coherent. When using only one BPR pair, the 500 m BPR pair (WBb6 and EBb3) yields a slightly better $AMOC_g'$ reconstruction than using the 300 m BPR pair (WBb5 and EBb2) on short and long time scales.

The sensitivity tests for the assumptions made regarding the vertical structure suggest that, firstly, the use of a level of no net motion across the basin is justified. Secondly, approximating the vertical structure by linear or spline interpolation considerably worsens the $AMOC_g'$ reconstruction compared to EOF regression. Thirdly, using only one instead of the two BPR pairs hardly worsens the $AMOC_g'$ reconstruction and adding a BPR pair at 1200 m depth only slightly improves the $AMOC_g'$

https://doi.org/10.5194/egusphere-2026-2983
Preprint. Discussion started: 12 June 2026

reconstruction.

3.2 Using moored temperature and salinity

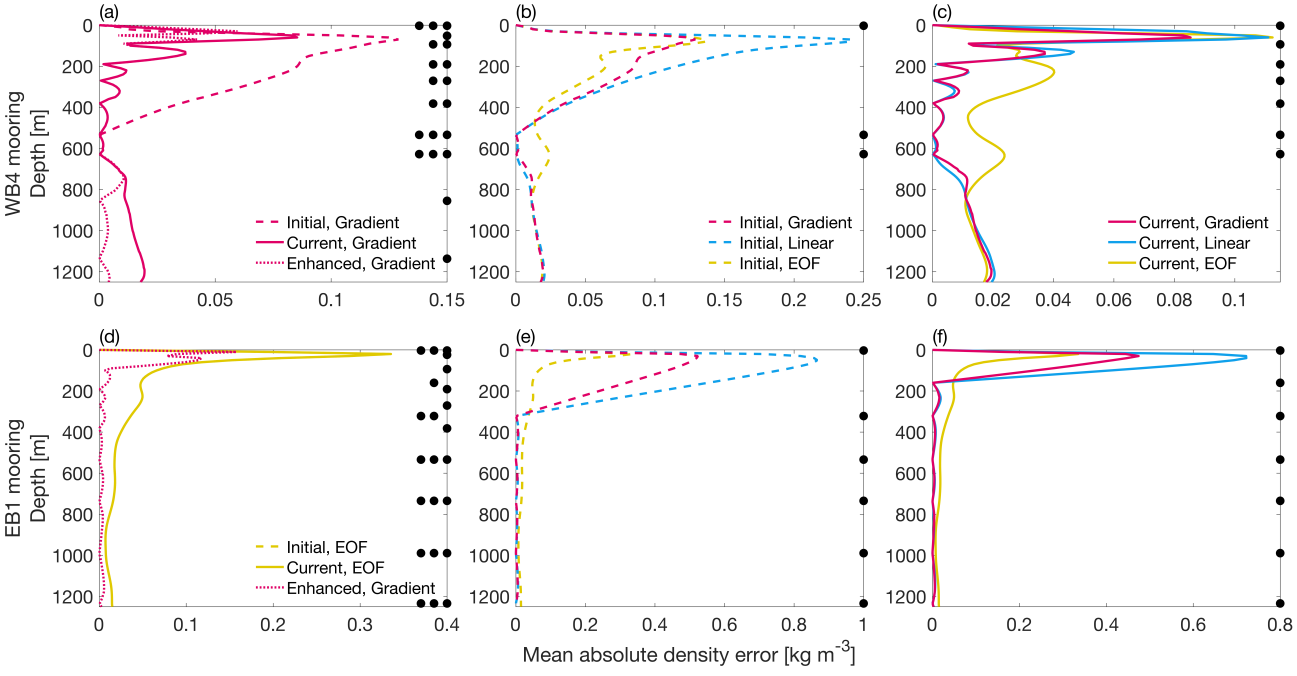

Figure 5. Time-mean absolute error of the reconstruction of density profiles with higher vertical resolution than the spacing of moored temperature and salinity measurements. Displayed are results for the moorings WB4 (a)-(c) and EB1 (d)-(f) considering different vertical setups (initial (dashed, m-wb4 #1 & m-eb1 #1), current (solid, m-wb4 #2 & m-eb1 #2), enhanced (dotted, m-wb4 #3 & m-eb1 #3)) and methods to approximate the vertical structure (stepwise integration of T&S using monthly climatological gradients (red, m-vst #1), linear interpolation of T&S anomalies (blue, m-vst #2), and EOF regression (yellow, m-vst #3)). For the EOF regression, the number of EOFs taken into account is chosen to achieve the best performance for each setup and mooring location, which results in using the first EOF in all cases except for the current WB4 mooring setup, where the first two EOFs are used. (a) and (d) show for each setup the best vertical method. (b) and (e) show the different vertical methods for the initial setup. (d) and (f) show the different vertical methods for the current setup. The dots on the right hand side indicate the positions of temperature and salinity measurements for the setups shown in the respective subplot. For the WB4 mooring (a)-(c), there is also a measurement at about 1900 m depth for all three setups which is not appearing in the figure. Note also the different scales of the x-axis.

For the moored temperature and salinity method, temperature (T) and salinity (S) measurements from the WB4 and EB1 moorings are used to calculate the interior transport of $AMOC_g$ in between the moorings, as described in section 2.4.2. The model-true boundary currents are then added to obtain and evaluate the basin-wide $AMOC_g$. The boundary currents alone (Table 6 - Case 1) only underestimate the model-true trend by 7 % and already explain a large part (62 %) of the $AMOC_g$

https://doi.org/10.5194/egusphere-2026-2983
Preprint. Discussion started: 12 June 2026

long-term variability, even though the rmse is higher than the std of the model truth. The boundary currents alone do not capture the $AMOC_g$ short-term variability, even though the mean seasonal cycle is quite accurately reconstructed. This implies that in VIKING20X the interior is particularly important for the $AMOC_g$ short-term variability and hardly important for the long-term variability. Before looking at the $AMOC_g$ reconstruction including the interior transport, the interpolation of the individual T&S measurements onto a higher-resolution vertical grid is assessed.

3.2.1 Reconstruction of vertically high-resolution density profiles

The absolute time-mean error of the reconstructed density profiles is compared for different vertical setups of sensors and for different methods to approximate the vertical structure (Fig. 5). The error in density reconstruction is generally largest in the upper ocean, associated with the depths of the strongest T&S gradients and variability (see Fig. C1). The maxima/minima of the T&S gradients are more pronounced, shallower, and more variable for the EB1 mooring location than for the WB4 mooring location. This makes the upper-layer reconstruction at the EB1 mooring location more uncertain. It is reflected in the higher density reconstruction errors for the EB1 mooring compared to the WB4 mooring, even when comparing a similar setup (enhanced, Fig. 5a+d). The density reconstruction error clearly decreases when more T&S measurements are taken into account, that is when the moorings are changed from the initial to the current setup (Fig. 5 b→c, e→f). Regardless of the selected setup and mooring, linear interpolation of T&S anomalies and stepwise integration of T&S using monthly climatological gradients have similar overall performance, with the latter exhibiting smaller errors particularly near the surface (approximately in the upper 200 m). This can be explained by seasonal variations in the vertical structure becoming important towards the surface, which are only considered for the latter method. EOF regression achieves, compared to the other two methods, the best results above the first instrument for a sparse setup (more precisely, this is the case for the initial setup for both moorings and for the extended setup for mooring EB1). However, the associated errors are still comparably high. Below the uppermost instrument, EOF regression performs worse than the other two methods for all setups. The comparison so far is idealised towards the surface as surface salinity measurements are assumed known. To be more realistic, we also assumed no surface salinity measurements and tested different methods of filling the gap between the uppermost instrument with salinity measurement and the surface (Fig. C2). The density reconstruction error is then minimal in the current setup and with a realistic surface salinity option for both WB4 and EB1 mooring when applying stepwise integration of T&S using climatological gradients and a surface salinity climatology. Hence, density profiles reconstructed by stepwise integration of T&S using climatological gradients and a surface salinity climatology will be taken in the following to calculate $AMOC_g$.

3.2.2 Reconstruction of $AMOC_g$

The interior part of $AMOC_g$ can then be calculated from the now vertically high-resolution density profiles either by integrating from the surface and taking SSH into account (Eq. (3) and Eq. (5)) or by integrating from a level of no net motion (here at 1100 m depth; Eq. (7)). For integrating from the surface, we assume in a first step one of the moorings as an idealised mooring

https://doi.org/10.5194/egusphere-2026-2983
Preprint. Discussion started: 12 June 2026

Table 6. Statistics for the simulated array-reconstruction of $AMOC_g$ compared to the model-true $AMOC_g$ based on the moored temperature and salinity (MTS) method. For explanations of the statistics and shading see Table 3. A legend for the assumptions used for the presented reconstructions is given by Table 2. For all cases, the vertical gaps between sensors are filled by stepwise integration of climatological gradients (m-vst #1) and at the surface, a salinity climatology is assumed (m-sur #1).

MTS Cases	Assumptions			High pass filtered		Monthly clim.		Low pass filtered		Linear trend (Sv decade^{-1})
	m-wb4	m-eb1	m-idr	rmse (Sv)	R	max-min (Sv)	month of max	rmse (Sv)	R	
model-truth				std 2.12		5.83	Jun	std 0.69		-1.08
1	boundary currents only			4.19	0.31	6.06	Jun	0.84	0.79	-1.00*
Integration from surface										
2	3	0	1	1.33	0.85	5.48	Jun	0.64	0.69	-1.04*
3	0	3		2.82	0.57	5.15	Jun	1.17	0.34	-0.64
Integration from 1100 m										
7	2	2	2	5.11	0.42	9.82	Mar	1.20	0.62	-0.39
8	3	2		5.09	0.41	9.59	Mar	0.55	0.78	-0.82*
EB1 relative to BPR										
12	3	2	3	1.45	0.83	5.56	Jun	0.61	0.81	-2.02
EB1 & WB4 relative to BPRs										
14	2	1	4	1.42	0.83	5.37	May	0.80	0.80	-1.02*

(assuming measurements at every vertical model level used) to separately evaluate the reconstructions based on the different WB4 and EB1 mooring setups. The enhanced setup is sufficient for the WB4 mooring to capture the $AMOC_g$ variability but not for the EB1 mooring where the density reconstruction error is just too high close to the surface (Table 6 - Cases 2 and 3). As the density reconstruction error for the EB1 mooring is too high to reconstruct $AMOC_g$ even for a setup with small sensor spacing (enhanced setup), integration from the surface is not a suitable approach regardless of the setup of the WB4 mooring. Using a climatological year for the EB1 mooring leads to a better but still not satisfying reconstruction of $AMOC_g$ with the linear trend being doubled in comparison to the model truth (Table B2 - Cases 4 to 6). This negative trend offset is likely caused by ignoring the negative pressure trend at the eastern boundary (similarly as discussed in section 3.1). The reconstruction of $AMOC_g$ short-term variability improves when the variability of the EB1 mooring is replaced by a climatological year; however, even when complemented with the enhanced setup for the WB4 mooring, the reconstruction is still inferior to that obtained for the bottom pressure method. When integrating from a level of no net motion (Table 6 - Cases 7 and 8), the impact of the high density reconstruction error close to the surface can be reduced. Still, the short-term variability cannot be reconstructed for any of the mooring setups, implying that a level of no net motion across the basin at 1100 m depth does not

https://doi.org/10.5194/egusphere-2026-2983
Preprint. Discussion started: 12 June 2026

hold at short (seasonal) time scales. The $AMOC_g$ long-term variability can be well reconstructed, if the WB4 mooring setup is changed to the enhanced setup in order to reduce the density reconstruction error below 650 m depth. The performance in reconstructing $AMOC_g$ long-term variability is slightly improved to that achieved when considering boundary currents alone. This is already a good result as it implies that the method is capable of indicating if there was also relevant long-term variability in the interior in the real ocean. Changing the EB1 mooring setup to the enhanced setup hardly improves the reconstruction (Table B2 - Case 9).

In summary, the TRACOS mooring array was not planned as a dynamic height array which resulted in a rather sparse (initial) distribution of T&S sensors which has recently been partly refined to the current setup. The reconstruction error of vertically high-resolution density profiles is similar when using the methods of linearly interpolating temperature and salinity anomalies and of stepwise integrating climatological temperature and salinity gradients (despite being different in complexity), though the latter showed an improved performance close to the surface. The salinity gap between the uppermost instrument and the surface was best filled when using climatological sea surface salinity. The resulting $AMOC_g$ reconstructions are not sufficient to capture short-term variability as good as the reconstructions based on the bottom pressure method. 61 % of the long-term variability can be explained when the interior part of $AMOC_g$ is calculated relative to a level of no net motion across the basin (here at 1100 m depth), provided that the setup of the WB4 mooring is further refined to the enhanced setup. Without this setup refinement, it remains best to determine the $AMOC_g$ long-term variability solely from the boundary currents, implying that then the desired signal-to-noise ratio (std/rmse > 1) cannot be achieved.

3.3 Using acoustic round-trip travel time

The acoustic round-trip travel time from IESs τ_{ies} is commonly used to reconstruct density profiles by applying the GEM technique, as described in section 2.4.3. We will explore the usability of this approach at the locations of the IESs WBb5, WBb6, and EBb4. Simulated travel times are related to density, both computed from yearly mean temperature and salinity profiles at the IESs locations. The relation of the two variables is displayed for some exemplary depth levels in Fig 6a-i. The cubic fits (transfer functions), which would lead to the look-up table, fit well with data around the depth of the thermocline; that is, around 300 m for IESs WBb4 and WBb5, and around 100 m for IES EBb4. Closer to the surface and at larger depths, there is no clear relationship making the fits unusable as transfer functions. The inadequacy of some of the fits also becomes apparent when looking at the time-mean absolute error when reconstructing yearly density profiles from the fits. These errors are maximum at the surface, reaching values of 0.37 $\mathrm{kg\,m^{-3}}$ for IES EBb4 and 0.15 $\mathrm{kg\,m^{-3}}$ for IESs WBb5 and WBb6 (not shown). Comparing these errors to the errors of the moored temperature and salinity method from section 3.2 indicates that the errors here are too high to reliably reconstruct geostrophic transport. These results confirm the doubts of Perez et al. (2011) that 11°S is not a suitable latitude for applying the GEM technique.

https://doi.org/10.5194/egusphere-2026-2983
Preprint. Discussion started: 12 June 2026

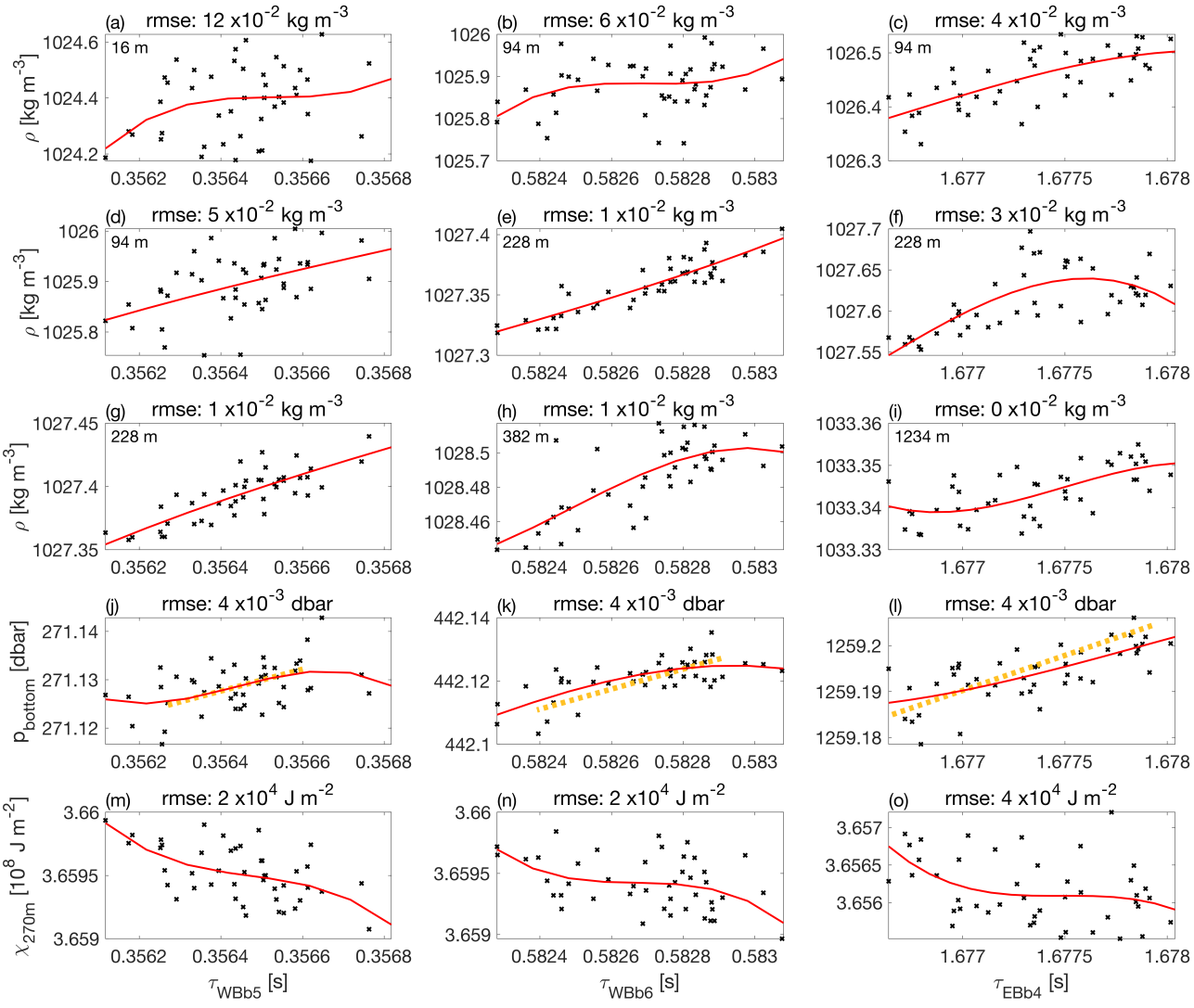

Figure 6. Potential transfer functions of acoustic round-trip travel time to desired reconstruction properties. Travel times are simulated for the WBb5 (left column), WBb6 (middle column), and EBb4 (right column) IES locations and related to (a)-(i) density for three exemplary depth levels for each IES, (j)-(l) bottom pressure, and (m)-(o) Fofonoff potential at 270 m depth. Each cross represents an annual mean. Cubic polynomials fitted to the data (potential transfer functions) are shown in red. For the bottom pressure values (j)-(l), the dashed yellow lines connect the starting and ending points of linear trends which were separately fitted to bottom pressure and travel time time series between 1994 and 2023.

https://doi.org/10.5194/egusphere-2026-2983
Preprint. Discussion started: 12 June 2026

While the GEM technique is not applicable due to a poor performance especially in the upper ocean, the travel time could more reliably relate to integrated quantities, for example to the bottom pressure and the Fofonoff potential. The fits of travel time to bottom pressure for the simulated hydrographic profiles (Fig. 6j-l) show some pattern with shorter (longer) travel times relating to lower (higher) bottom pressure. The fits for the transfer function further resemble the slope connecting the start and end points of linear trends fitted separately to the bottom pressure and the travel time series between 1994 and 2023. While this suggests that the travel time data contain some information about the long-term variability of bottom pressure, annual bottom pressure values are highly variable with respect to travel time data, thereby limiting the usefulness of these fits as transfer functions. A reconstruction of bottom pressure based on these transfer functions (Fig. D1a+c purple) would hardly capture the long-term pressure variability with correlations to the model truth of 0.44 (0.57) for the location of WBb5 (WBb6). A linear trend in bottom pressure would be underestimated at both sites by about 30 %. The fits for the Fofonoff potential (Fig. 6m-o) do not show a clear relation to the travel time. This is the case for both χ_{270m} (depth range of WBb5 IES) and χ_{440m} (depth range of WBb6 IES, not shown). The reason for the worse relation of travel time to Fofonoff potential compared to the bottom pressure is probably due to the higher influence of surface variability in computing the Fofonoff potential. Following from these results, travel time measurements at 11°S do not seem suitable to be incorporated in the reconstruction of geostrophic transports and, hence, $AMOC_g$.

3.4 Combination of data sets and methods to optimally compute the AMOC at 11°S

The previous sections (3.1, 3.2, and 3.3) showed that none of the presented methods and data sets alone is optimal to reconstruct $AMOC_g$ variability at 11°S. The bottom pressure method could capture the $AMOC_g$ variability well if not suffering from two major limitations: 1) the pressure sensor drift omitting $AMOC_g$ long-term variability and 2) the EB data gaps additionally reducing the performance in reconstructing $AMOC_g$ short-term variability. The moored temperature and salinity method could capture the $AMOC_g$ long-term variability well, provided that the WB4 mooring setup is further refined. Otherwise, boundary currents alone can account for a large part of the $AMOC_g$ long-term variability, albeit with a high level of noise. The reconstruction of $AMOC_g$ short-term variability by the moored temperature and salinity method is clearly worse than the reconstruction by the bottom pressure method. IESs do not seem suitable to be incorporated in the $AMOC_g$ reconstruction at 11°S. Now, bottom pressure and moored temperature and salinity data and methods will be combined to improve the $AMOC'_g$ reconstruction.

For the eastern boundary, the EB1 mooring and EBb4 BPR are co-located and thus their data can be combined by rearranging Eq. (5):

$$p(z,t) = p(1200\,m,t) - g \cdot \int_{1200m}^{z} \rho(z',t)\,dz' \tag{8}$$

https://doi.org/10.5194/egusphere-2026-2983
Preprint. Discussion started: 12 June 2026

Table 7. Statistics for the simulated array-reconstruction of $AMOC'_g$ compared to the model-true $AMOC'_g$ based on the bottom pressure method combined with moored temperature and salinity data. For explanations of the statistics and shading see Table 3. A legend for the assumptions used for the presented reconstructions is given by Table 1. For the cases displayed in this table, only assumptions regarding sensor drift (b-prc) and EB data gaps (b-ebb) vary, while other parameters are unchanged (b-ref #1, b-vst #1, b-stp #1).

BPR Cases	Assumptions		High pass filtered		Monthly clim.		Low pass filtered		Linear
	b-prc	b-ebb	rmse (Sv)	R	max-min (Sv)	month of max	rmse (Sv)	R	trend (Sv decade^{-1})
model-truth			std 2.12		5.83	Jun	std 0.69		-1.08
1 ('idealised')	0	0	1.06	0.91	7.76	Jun	0.16	0.98	-0.73
9 ('current')	1	1	1.82	0.75	9.11	May	0.73	-0.02	-0.14
Moored T&S for EB									
21	0	2	1.33	0.89	8.91	Jun	0.23	0.96	-0.53
Moored T&S for WB									
22	5a	0	1.56	0.81	7.48	Jun	0.58	0.60	-0.94*
23	5b	0	1.32	0.86	7.47	Jun	0.53	0.64	-0.94*

where $\rho(z',t)$ is a vertically high-resolved density profile which can be generated using the stepwise integration approach for the initial setup of the EB1 mooring as described in section 2.4.2 and used in section 3.2. When the drift problem is taken into account and a de-drifted BPR at 1200 m is simulated, the density contribution is high-pass filtered with a 2 year cut-off to better match the variability of the BPR and to not introduce some artificial longer-term variability signal which would otherwise cancel out. Equation (8) can be used to tackle the EB data gaps in the BPR based method. Note that using the pressure of the EB1 mooring as boundary pressure generates a bottom triangle whose impact on $AMOC'_g$ is, however, assumed to be small due to the weak eastern boundary circulation. The corresponding reconstruction of the pressure of the EB1 mooring at 300 m and 500 m depth (Fig. D1b+d) is slightly more accurate at 500 m depth with an rmse of 0.003 dbar and a Pearson correlation coefficient of 0.94 than at 300 m depth with an rmse of 0.004 dbar and a correlation coefficient of 0.91. According to a Lilliefors test, both errors are nearly normally distributed around zero.

Implementing this pressure derivation to the $AMOC'_g$ reconstruction implies for the bottom pressure method that the EBb1 and EBb2 data gaps can be replaced by the pressure derived from Eq. (8) (Table 7 - Case 21). The performance of the resulting $AMOC'_g$ short-term variability is improved compared to the performance of the reconstruction filling the EB data gaps by annual and semi-annual harmonics (Table 7 - Case 9) and almost matches the performance of the reconstruction based on the original EB BP values (Table 7 - Case 1). Hence, with the EB1 mooring and the BPR at 1200 m (EBb4), the eastern boundary pressure can be successfully reconstructed and the additional overestimation of the $AMOC'_g$ seasonal cycle caused by the EB

https://doi.org/10.5194/egusphere-2026-2983
Preprint. Discussion started: 12 June 2026

data gaps in the current setup can be reduced.

For the western boundary, the bottom pressure along the continental slope and the pressure profile of the WB4 mooring can be linked by taking into account the zonal pressure gradient caused by the western boundary current (basically adapting Eq. (3)):

$$p_{WB}(z,t) = p_{WB4}(z,t) - f \cdot \rho_0 \cdot \int_{WB}^{WB4} v(x,z,t)\, dx \tag{9}$$

where p_{WB4} is computed following Eq. (5). This approach is basically an application of the stepping method by Hughes et al. (2013) with one step and has the potential to overcome the issue of pressure sensor drift at the western boundary for the bottom pressure method. The corresponding reconstruction of WBb5 and WBb6 pressure (Fig. D1a+c yellow and red) is slightly more accurate at 300 m depth than at 500 m depth and more accurate considering the enhanced than the current setup of the WB4 mooring. For the long-term variability (> 5 years, linear trend removed), the Pearson correlation coefficients amount to 0.66 (300 m / WBb5 BPR) and 0.57 (500 m / WBb6 BPR) when using the current setup of the WB4 mooring, and to 0.84 (300 m / WBb5 BPR) and 0.77 (500 m / WBb6 BPR) when using the enhanced setup of the WB4 mooring and thus when assuming an additional measurement at 50 m depth. Linear trends would be underestimated by 7 % for both BPRs and considering both mooring setups. According to a Lilliefors test, the errors are nearly normally distributed around zero.

Implementing this pressure derivation to the $AMOC'_g$ reconstruction means for the bottom pressure method that the WBb5 and WBb6 BPRs are replaced by the pressure derived from Eq. (9) (Table 7 - Cases 22 and 23). The performance of the resulting $AMOC'_g$ short-term variability is slightly reduced compared to the performance considering the actual bottom pressure. The performance of the resulting $AMOC'_g$ long-term variability is clearly improved compared to the performance considering actual but de-drifted BPRs. Further refining the WB4 mooring setup from current to enhanced slightly improves the reconstruction of long-term variability. However, with only 41 % of the long-term variability being explained, this approach is still worse than reconstructing the $AMOC'_g$ long-term variability by the boundary currents alone (Table 7 - Case 1), even though the rmse is smaller.

For the moored temperature and salinity method, the combination with de-drifted bottom pressure measurements has the potential to improve the short-term variability of the pressure profiles of the WB4 and EB1 moorings. In a first step, Eq. (8) is utilised, as above, to reconstruct the pressure profile of the EB1 mooring, which simultaneously leads to omitting the long-term variability at the eastern boundary. Then, $AMOC'_g$ can be computed by integrating from the bottom for the EB1 mooring and from the surface for the WB4 mooring. The performance of the resulting $AMOC'_g$ (Table 6 - Case 12) short-term variability is good and gets comparable to the performance of the bottom pressure method provided that the WB4 mooring setup is refined to enhanced. Changing the setup of the EB1 mooring hardly impacts the performance of reconstruction (Table B2 - Cases 10 to 13). The performance of the resulting $AMOC'_g$ long-term variability equals the performance of the reconstruction based

https://doi.org/10.5194/egusphere-2026-2983
Preprint. Discussion started: 12 June 2026

on a climatological year for the EB1 mooring (Table B2 - Cases 4 to 6) with the linear trend being doubled in comparison to the model truth. In a second step, the WBb6 BPR can be utilised to reconstruct the pressure of the WB4 mooring at about 500 m depth by rearranging Eq. (9). The pressure profile of the WB4 mooring can then be computed by adapting Eq. (8), with the pressure contribution from the western boundary current being high-pass filtered with a 2 year cut-off to fit to the de-drifted BPR data and, hence, the long-term variability at the western boundary of the interior is also omitted. The resulting $AMOC'_g$ reconstruction (Table 6 - Case 14) no longer contains any long-term variability from the interior. The performance of the $AMOC'_g$ short-term variability nearly equals the performance of the first step in which the pressure profile of the WB4 mooring was still referenced to the surface and not to BPR data. The advantage here is that the setup of the WB4 mooring can be less refined and the current setup instead of the enhanced setup is sufficient (cf. Table B2 - Cases 14 and 15). However, for reconstructing short-term variability (< 2 years) based on a combination of bottom pressure and moored temperature and salinity data, approaches based on the moored temperature and salinity method cannot outperform those based on the bottom pressure method.

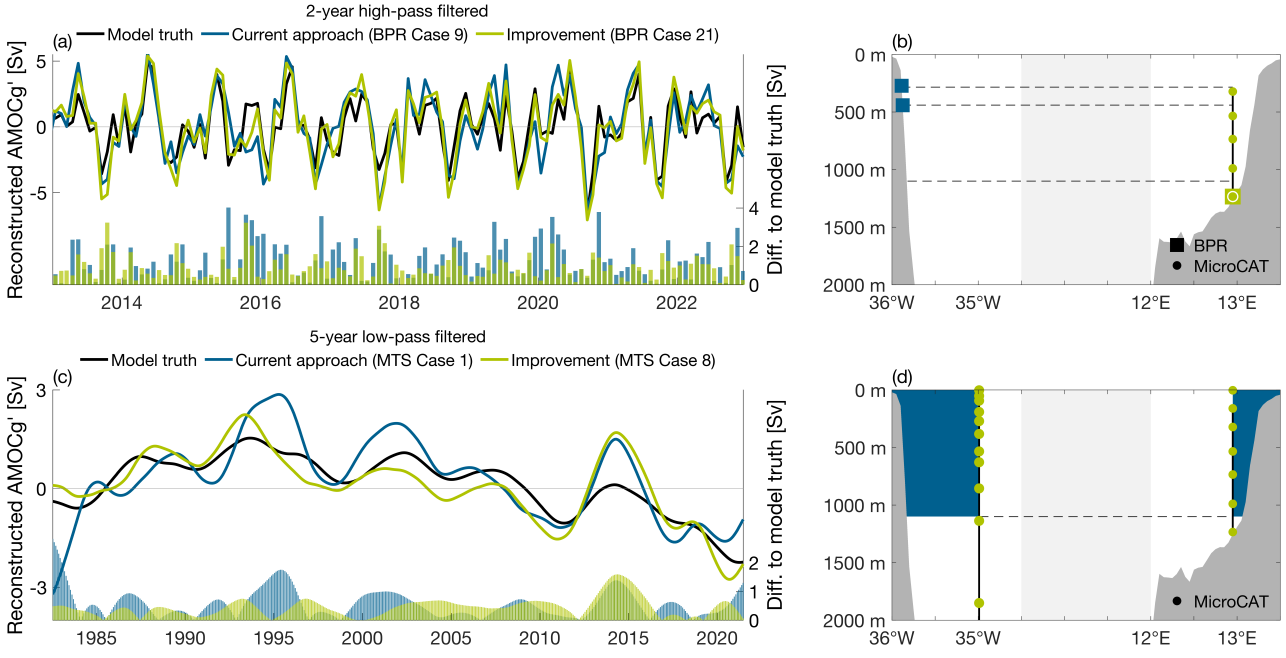

Figure 7. Performance of $AMOC'_g$ reconstruction from the TRACOS array based on the current approach (blue) and one possible improvement (light green). Reconstructions are separately evaluated for both short-term (< 2 years, top) and longer-term (> 5 years, bottom) variability. (left): Time series of the reconstructed $AMOC'_g$ and difference to the model truth. (right): Schematics of instruments used for the shown reconstructions. Note that for (a) only the last ten years of the time series are shown exemplary.

https://doi.org/10.5194/egusphere-2026-2983
Preprint. Discussion started: 12 June 2026

To summarise, we found different approaches for successfully reconstructing $AMOC'_g$ short-term and long-term variability with the latter appearing more difficult to reconstruct. For the short-term variability, the reconstruction is currently based on the bottom pressure method whereby suffering from EB data gaps (Fig. 7a+b blue). The reconstruction can be improved when filling the EB data gaps by the EB1 mooring and EBb4 BPR (Fig. 7a+b yellow), allowing to capture 79 % of the short-term variability. This approach cannot be outperformed by the moored temperature and salinity method but nearly similar performance can be achieved when integrating the pressure profiles of the WB4 and EB1 moorings relative to the BPRs WBb6 and EBb4 respectively (Table 6 - Cases 12 and 14). The poorer performance regarding rmse and correlation is, however, countered by a more accurate representation of the amplitude of a monthly climatology. For the long-term variability, the reconstruction is currently solely based on direct measurements of the boundary currents whereby suffering from missing out any potential longer-term variability in the interior (Fig. 7c+d blue). The reconstruction can be improved when adding the variability of the interior between the WB4 and EB1 moorings, provided that the WB4 mooring setup is further refined to enhanced (Fig. 7c+d yellow), allowing to capture 61 % of the long-term variability. When only the current setup for the WB4 mooring is given, still some of the long-term variability in the interior can be captured when reconstructing the WBb5 and WBb6 BPRs by the WB4 mooring and western boundary current (Table 7 - Case 22). This approach leads to a better performance regarding rmse but a worse performance regarding correlation compared to the current approach with using boundary currents alone.

4 Discussion and Conclusion

This study conducts an observing system simulation experiment (OSSE) for the TRACOS observational array at 11°S as an AMOC observing system. With that, we assess the uncertainty and potential of the TRACOS array to capture AMOC short-term (seasonal to interannual, < 2 years) and long-term (decadal to multi-decadal, > 5 years) variability based on currently used and alternative approaches. So far, the TRACOS array has been used to capture the AMOC short-term variability (Herrford et al., 2021) and the transport of the boundary currents (Hummels et al., 2015; Kopte et al., 2017). Both approaches are subsampled here from the output of an ocean model simulation. For the first approach (in this study called bottom pressure method), two bottom pressure recorders (BPRs) at each side of the basin are used to reconstruct geostrophic AMOC transport ($AMOC_g$), explaining 56 % of the short-term variability while overestimating the amplitude of the mean seasonal cycle by 56 %. Similar results can be achieved when using only one BPR at each side of the basin. However, this method suffers from two major limitations: pressure sensor drift and data gaps at the eastern boundary (EB). The pressure sensor drift requires de-drifting of the pressure time series which basically acts as a high-pass filter with the deployment length setting the cut-off period. Given the current deployment lengths of around two years, pressure sensor drift makes it impossible to detect long-term variability. Data gaps at the EB additionally induced uncertainty for the short-term variability. For the second approach, direct observation of the boundary currents can already explain 62 % of the basin-wide $AMOC_g$ long-term variability, with, however, the root mean squared error exceeding the underlying variability defined by the standard deviation. The $AMOC_g$ long-term variability

https://doi.org/10.5194/egusphere-2026-2983
Preprint. Discussion started: 12 June 2026

is generally harder to reconstruct than the short-term variability due to its smaller amplitude.

The dominance of the (western) boundary currents for the $AMOC_g$ long-term variability has already been indicated in a previous model study. Rühs et al. (2015) found that the North Brazil Undercurrent captures the basin-scale decadal to multi-decadal AMOC variability provided that wind-driven gyre changes are accounted for. Similarly, previous model studies (Bingham and Hughes, 2008, 2009) and observational studies (Elipot et al., 2014) pointed out the dominance of the western boundary pressure for $AMOC_g$ long-term variability. We find that when ignoring the long-term pressure variability at the EB, nearly 50 % of the long-term variability can still be explained, however, the impact on a trend seems more complicated. The interest in possible contributions from the interior to $AMOC_g$ long-term variability is further raised by a recent assessment of the RAPID array components showing that observing the upper 1000 m of the eastern boundary is relevant for observing the AMOC trend (Petit et al., 2025). In any case, at 11°S the interior is important for the shorter-term variability which is dominated by seasonal westward propagating Rossby waves (Döös, 1999; Herrford et al., 2021). A comparison of the simulated array-reconstructed $AMOC_g$ in VIKING20X with the observational $AMOC_g$ estimate from Herrford et al. (2021) shows that the seasonal cycle amplitude for the period 2013-2018 is 23 % smaller in the model (underestimation of 49 % when comparing the model-true $AMOC_g$ instead of the array-reconstructed $AMOC_g$ with the observational estimate). Hence, discrepancies in the seasonal representation of the AMOC between models and observations remain, even when taking the methodological bias of the observational strategy into account. This might point to a model bias whose correction could help to also reduce the uncertainty in AMOC projections (Bonan et al., 2025).

Alternative approaches which were tested to compute $AMOC_g$ from the TRACOS array include 1) the implementation of BPRs with the A-0-A technology for self-calibration of the pressure sensor drift, 2) a RAPID- and OSNAP-like approach with moored temperature and salinity measurements for the interior, 3) a SAMBA-like approach based on acoustic round-trip travel times, and 4) the implementation of moored temperature and salinity data into the bottom pressure approach. We find that:

1) The currently remaining nominal drift rates of the A-0-A BPRs may still be too high to observe a linear $AMOC_g$ trend of 1 $\mathrm{Sv\,decade^{-1}}$. It should be noted that the ability of A-0-A BPRs to detect an $AMOC_g$ trend is also impacted by settling of the instrument into the seafloor (Harmon et al., 2026) and by possible geophysical processes (vertical seafloor movement; probably small for the BPRs WBb5 and WBb6 as they are located at the continental slope in the Alagoas basin at a transitional passive continental margin with likely little subsidence) obscuring oceanographic trends. Hence, statements about $AMOC_g$ long-term variability - particularly regarding the $AMOC_g$ trend - remain challenging based on BPRs, even when considering A-0-A BPRs. While we are unsure about the advantage of A-0-A BPRs with non-negligible remaining drifts over standard BPRs, we want to highlight again the advantage of long BPR deployments as their length sets the periods of observable variability and as this reduces the impact of instrument settling which occurs with each deployment.

https://doi.org/10.5194/egusphere-2026-2983
Preprint. Discussion started: 12 June 2026

2) The $AMOC_g$ long-term variability can be reconstructed when combining the boundary current transports with the interior transport derived from pressure profiles of WB4 and EB1 moorings integrated relative to a level of no net motion. However, for the reconstruction being more accurate than the one considering boundary currents only, it is necessary that the setup of the WB4 mooring is further refined (to the enhanced setup; involving three more sensors compared to the current setup and then matching spacing requirements outlined in McCarthy et al. (2015)). Doing so, 61 % of the $AMOC_g$ long-term variability can be explained. While the explained variability is not much improved compared to using boundary currents alone, the root mean squared error is almost halved and potential long-term variability in the interior is accounted for.

3) The acoustic round-trip travel times have low skill reconstructing yearly bottom pressure and yearly density around the depth of the thermocline. In the real ocean, the reconstruction is even more difficult and expected to be more noisy, as there are no idealised lookup tables available (lookup tables will be made up of fewer and horizontally spread profiles) and as the sensors are deployed quite shallow with 300 m and 500 m depth. Hence, acoustic round-trip travel times may not be suitable for geostrophic transport calculations at 11°S. However, the suggested approach of using acoustic round-trip travel times to reconstruct yearly bottom pressure to overcome the issue of pressure sensor drift is likely promising at other latitudes (e.g., 34.5°S) with a larger dynamic height anomaly range and a higher signal-to-noise ratio (Perez et al., 2011).

4) The EB data gaps in the bottom pressure method can be successfully filled by combining a BPR at 1200 m (EBb4) with the EB1 mooring. Doing so, 79 % of the $AMOC_g$ short-term variability can be explained. The long-term variability of the western boundary BPRs can be recovered by combining the pressure profile of the WB4 mooring with the western boundary current velocities. This approach is basically an adaptation of the stepping method of Hughes et al. (2013). Doing so, 40 % of the $AMOC_g$ long-term variability can be explained. While we seem to be able to recover linear bottom pressure trends over a 30-year period with an accuracy of $\pm$ 0.04 $\mathrm{mm\,year^{-1}}$, Williams et al. (2015) found that when accounting for the vertical setup of the mooring as well as the measurement uncertainty, a trend in bottom pressure at 26°N can be detected to an accuracy of $\pm$ 1 $\mathrm{mm\,year^{-1}}$ after 12 years. Similarly, moorings at 16°N and 26°N were found to be able to reconstruct trends in steric sea level with an accuracy of 0.7 $\mathrm{mm\,year^{-1}}$ to 0.9 $\mathrm{mm\,year^{-1}}$ over 12 to 13-year periods when accounting for instrumental error and calibration error (Koelling et al., 2020). The difference in accuracy found in this study compared to previous studies likely results from the (non-)accounting of measurement uncertainty, even though the length of observation and the geographical location might also play a role. Regardless, it can be stated that the $AMOC_g$ reconstruction at 11°S can be improved when combining the bottom pressure and moored temperature and salinity data.

The applicability of the OSSE results to the real ocean depends on the accuracy of the realism of the used ocean model simulation VIKING20X. While the model is dynamically consistent and has been validated regarding the representation of the AMOC, three biases have been identified. First, the used model possibly overestimates the mean of the western boundary

https://doi.org/10.5194/egusphere-2026-2983
Preprint. Discussion started: 12 June 2026

currents. Hence, the relative importance of the boundary currents compared to the interior might be slightly reduced in the real ocean. Second, the used model underestimates the amplitude of the seasonal cycle, even when considering the methodological overestimation which became apparent in this study. Hence, the ratio of seasonal signal to long-term signal is even larger in the real ocean, making longer-term variability even more masked and thus harder to observe following a signal to noise framework (McCarthy et al., 2025). Third, the used model does not include global steric sea level rise. Hence, the real trends of SSH and bottom pressure might be more positive and the offset of a linear $AMOC_g$ trend when ignoring the EB long-term variability might be different in the real ocean.

Previous OSSEs of AMOC observing systems indicated the reference level bias, unsampled regions, and neglected ageostrophic transport as the main sources of uncertainty (e.g., Sinha et al., 2018). For the $AMOC_g$ reconstructions in this study:

- Utilising a level of no net motion (at approximately the interface between northward flowing Antarctic Intermediate Water and southward flowing upper North Atlantic Deep Water) seems justified. For the bottom pressure method, the error resulting from employing a level of no net motion instead of known motion is negligible. As also seen in former studies at 11°S (Herrford et al., 2021; Tuchen et al., 2022), the $AMOC_g$ reconstruction is not sensitive to shifting the level of no net motion by 200 m up or down. However, using a predefined level of no net motion might become problematic in the future as a weakened AMOC is expected to go along with a shallower overturning depth (Bonan et al., 2025).

- We approximate the AMOC as the sum of the Ekman transport and $AMOC_g$. This leaves a neglected ageostrophic component where the North Brazil Undercurrent hits the topography, indicating that the boundary currents are not entirely geostrophic, fitting results from earlier studies at 11°S (Baehr et al., 2009). However, this neglected ageostrophic component is small and is believed to not have an impact on the results presented here. As the direct current measurements in the real ocean also include ageostrophic velocities, the effect of the geostrophic and ageostrophic component could be disentangled.

- We rather identify the vertical structure and the filling of vertical gaps between the instruments (undersampled regions) as a main source of uncertainty. However, this effect has not been considered in multiple previous OSSEs where idealised moorings are subsampled (e.g., for the South Atlantic: Baehr et al., 2009; Perez et al., 2011). Note that while this study aimed to assess the performance of the TRACOS array as realistic as possible, still some aspects remain idealised and are beyond the scope of this study, including measurement uncertainty apart from the pressure sensor drift, the accuracy of drift removal, and the effect of non-harmonic tides on the pressure time series and internal tides on temperature and salinity measurements. At least for the reconstructions based on moored temperature and salinity data, however, the measurement errors were previously found to be clearly smaller than errors induced by the vertical setup of the mooring (Williams et al., 2015).

https://doi.org/10.5194/egusphere-2026-2983
Preprint. Discussion started: 12 June 2026

The assessment of the $AMOC_g$ computation at 11°S presented here is thought to be a necessary basis for both the observational and the modelling community when comparing to the current or future AMOC time series at 11°S. The established algorithm (Hans et al., 2026) can also be used to test further modifications of the TRACOS array setup. While this study focusses entirely on the computation of the AMOC as a zonally integrated transport and thus lacks the applicability for meridional heat and freshwater transport computations, the volume transport estimates and its uncertainty quantification are essential to validate another approach with meridional velocities on a zonal grid. The results presented here indicate that the TRACOS array is able to reconstruct $AMOC_g$ variability on short and long time scales by combining different types of measurements for the upper limb of the AMOC, even though the array setup is rather sparse. Some of the presented approaches might also be helpful for other arrays aiming for a reduced setup, even though an individual and careful assessment of changes in the level of accuracy is necessary and at higher latitudes the computation in density-space is required, limiting the applicability of the bottom pressure method as applied at 11°S. The findings regarding the potential and limitations of the bottom pressure method also have implications for the usability of 1) SMART (Science Monitoring And Reliable Telecommunications) cables and 2) satellite gravimetry. 1) SMART cables are telecommunication cables which are equipped with sensors, such as BPRs, aiming to monitor climate change including AMOC changes (Howe et al., 2019). For cables at lower latitudes, $AMOC_g$ can be derived following the bottom pressure method presented in this study. At high latitudes, the derivation of $AMOC_g$ from BPRs is less straight forward as isopycnals are tilted against isobars but there is also potential of SMART pressure sensors, e.g., in the subpolar North Atlantic (Goldberg et al., 2025). Given the limitations arising from pressure sensor drift (likely persisting even when considering current A-0-A BPR technology), an $AMOC_g$ trend of 1 $\mathrm{Sv\,decade^{-1}}$ might not be identifiable with BPRs on SMART cables and other measurements may need to be combined. However, the long deployment of SMART cables is a strong advantage allowing to capture longer-term variability. 2) Satellite gravimetry, including future missions, averages pressure signals over rather large areas, as for example outlined in Shihora et al. (2025). Our findings on the usability of only one pair of BPRs and a quite coherent pressure signal at least across the upper 1000 m of the continental shelf underlines the potential for satellite gravimetry to monitor $AMOC_g$ changes.

Code and data availability. The subset of the output of the VIKING20X model configuration (internally named VIKING20X.L46-KFS003) which is used in this study is available through GEOMAR (simulation data are in the process of publication). The scripts that were used for the analyses and figures are available in Hans et al. (2026). Further used toolboxes are CDFTOOLS version 4 (https://github.com/meom-group/CDFTOOLS, downloaded 2024) for computing bottom pressure and geostrophic velocities from the model output and the seawater library version 3-3.1 (Morgan and Pender, 2014). Colour maps from Thyng et al. (2016) and Crameri (2023) are used for figures to prevent visual distortion of the data and exclusion of readers with colour-vision deficiencies.

https://doi.org/10.5194/egusphere-2026-2983
Preprint. Discussion started: 12 June 2026

Appendix A: Differences in instrument depth of the TRACOS array between reality and model

Table A1. Difference between reality and model in the depth of instruments of the TRACOS array used in this study. Ranges indicate the depth variation of the respective instrument during different deployments. Brackets indicate the planned deployment depth if the instrument is not yet in the water.

	Depth of actual measurement	Depth subsampled in model
PIES/BPRs:		
WBb5	300 m to 320 m	272 m
WBb6	490 m to 530 m	441 m
WBb7	(1200 m)	1105 m
EBb2	300 m	295 m
EBb3	500 m	439 m
EBb4	1225 m	1252 m
MicroCATs on moorings:		
WB4	100 m, 200 m, 300 m, 400 m, 500 m, 650 m, 1900 m	94 m, 191 m, 271 m, 382 m, 534 m, 628 m, 1850 m
EB1	150 m, 300 m, 500 m, 700 m, 950 m, 1200 m	160 m, 322 m, 534 m, 735 m, 989 m, 1234 m

Appendix B: Extended statistics for the simulated array-reconstruction of $AMOC_g$ compared to the model-true $AMOC_g$

For better readability, reduced versions of the statistic tables are shown in the paper. Here, we present the tables with additional cases (lines) as well as columns for the rmse and R for the performance over the full time series. For the moored temperature and salinity method, here is also an additional column for the time-mean transport.

https://doi.org/10.5194/egusphere-2026-2983
Preprint. Discussion started: 12 June 2026

Table B1. Statistics for the simulated array-reconstruction of $AMOC_g$ compared to the model-true $AMOC_g$ based on the bottom pressure method. For explanations of the statistics and shading see Table 3. A legend for the assumptions is given by Table 1.

BPR Cases	Assumptions (b-)					Full time series		High pass filtered		Monthly clim.		Low pass filtered		Linear
	prc	ebb	ref	vst	stp	rmse (Sv)	R	rmse (Sv)	R	max-min (Sv)	month of max	rmse (Sv)	R	trend (Sv decade^{-1})
model-truth						std 2.49		std 2.12		5.83	Jun	std 0.69		-1.08
1	0	0	1	1	1	1.24	0.92	1.06	0.91	7.76	Jun	0.16	0.98	-0.73
Drift problem														
2	1	0	1	1	1	1.54	0.84	1.10	0.90	7.77	Jun	0.74	-0.05	-0.08
3	2					1.51	0.85	1.06	0.91	7.73	Jun	0.76	-0.19	-0.09
4	3a					1.23	0.92	1.06	0.91	7.76	Jun	0.16	0.98	8.81
5	3b					1.23	0.92	1.06	0.91	7.76	Jun	0.16	0.98	4.04
6	3c					1.24	0.92	1.06	0.91	7.76	Jun	0.16	0.98	-0.39
7	3d					1.24	0.92	1.06	0.91	7.76	Jun	0.16	0.98	-0.68
EB data gaps														
8	0	1	1	1	1	2.16	0.77	1.80	0.76	9.04	May	0.52	0.70	-1.06*
9	1	1				2.25	0.72	1.82	0.75	9.11	May	0.73	-0.02	-0.14
Depth z_{max}														
10	0	0	2	1	1	1.29	0.91	1.10	0.91	7.85	Jun	0.17	0.97	-0.70
11			3			1.24	0.92	1.07	0.92	7.77	Jun	0.16	0.98	-0.81
Approximate vertical structure														
12	0	0	1	2	1	1.14	0.92	0.98	0.92	7.20	Jun	0.16	0.97	-0.76
13				3		3.22	0.76	2.69	0.77	13.21	Jun	0.38	0.83	-0.81*
14				4		6.54	0.54	5.41	0.57	18.35	Jun	1.06	0.21	-0.90*
Setup modifications														
15	0	0	1	1	2	1.33	0.92	1.15	0.92	7.80	Jun	0.20	0.96	-0.89
16				1	3	1.40	0.89	1.21	0.88	8.01	Jun	0.21	0.95	-0.66
17				3	4	3.08	0.78	2.56	0.80	12.38	Jun	0.39	0.83	-0.89*
18				2	4	1.13	0.92	0.97	0.92	7.19	Jun	0.15	0.98	-0.76
19				5	4	1.38	0.91	1.18	0.91	8.23	Jun	0.23	0.95	-0.76
20				5	5	1.55	0.93	1.37	0.92	8.11	Jun	0.28	0.95	-1.09*
Merging moored T&S														
21	0	2	1	1	1	1.57	0.89	1.33	0.89	8.91	Jun	0.23	0.96	-0.53
22	5a	0				2.08	0.77	1.56	0.81	7.48	Jun	0.58	0.60	-0.94*
23	5b	0				1.69	0.84	1.32	0.86	7.47	Jun	0.53	0.64	-0.94*

https://doi.org/10.5194/egusphere-2026-2983
Preprint. Discussion started: 12 June 2026

Table B2. Statistics for the simulated array-reconstruction of $AMOC_g$ compared to the model-true $AMOC_g$ based on the moored temperature and salinity (MTS) method. For explanations of the statistics and shading see Table 3. A legend for the assumptions used for the presented reconstructions is given by Table 2. For all cases, the vertical gaps between sensors are filled by stepwise integration of climatological gradients (m-vst #1) and at the surface, a salinity climatology is assumed (m-sur #1).

MTS Cases	Assumptions (m-)			Full time series		High pass filtered		Monthly clim.		Low pass filtered		Linear trend	Time mean
	wb4	eb1	idr	rmse (Sv)	R	rmse (Sv)	R	max-min (Sv)	month of max	rmse (Sv)	R	(Sv decade^{-1})	(Sv)
model-truth				std 2.49		std 2.12		5.83	Jun	std 0.69		-1.08	25.74
1 (boundary currents only)				4.74	0.39	4.19	0.31	6.06	Jun	0.84	0.79	-1.00*	17.83
Integration from surface													
2	3	0	1	1.80	0.82	1.33	0.85	5.48	Jun	0.64	0.69	-1.04*	25.31
3	0	3		3.65	0.52	2.82	0.57	5.15	Jun	1.17	0.34	-0.64	25.08
4	0	4		2.07	0.75	1.73	0.73	5.70	Jun	0.67	0.83	-2.04	24.95
5	2	4		3.12	0.58	2.46	0.57	5.54	Jun	0.80	0.71	-2.11	25.16
6	3	4		2.55	0.68	2.07	0.66	5.53	Jun	0.63	0.81	-2.00	25.04
Integration from 1100 m													
7	2	2	2	5.66	0.47	5.11	0.42	9.82	Mar	1.20	0.62	-0.39	21.72
8	3	2		5.44	0.45	5.09	0.41	9.59	Mar	0.55	0.78	-0.82*	22.20
9	3	3		5.45	0.45	5.10	0.40	9.79	Mar	0.52	0.83	-0.81*	22.28
EB1 relative to BPR													
10	2	1	3	2.82	0.67	2.14	0.71	5.69	Jun	0.78	0.71	-2.12	17.83
11	2	2		2.64	0.69	1.96	0.73	5.56	Jun	0.77	0.71	-2.13	17.83
12	3	2		1.93	0.81	1.45	0.83	5.56	Jun	0.61	0.81	-2.02	17.83
13	3	3		1.90	0.82	1.41	0.84	5.52	Jun	0.61	0.81	-2.02	17.83
EB1 & WB4 relative to BPRs													
14	2	1	4	2.16	0.77	1.42	0.83	5.37	May	0.80	0.80	-1.02*	17.83
15	3	3		2.17	0.78	1.43	0.83	5.39	May	0.79	0.80	-1.02*	17.83

https://doi.org/10.5194/egusphere-2026-2983
Preprint. Discussion started: 12 June 2026

Appendix C: Vertical structure for reconstructing density profiles for WB4 and EB1 moorings

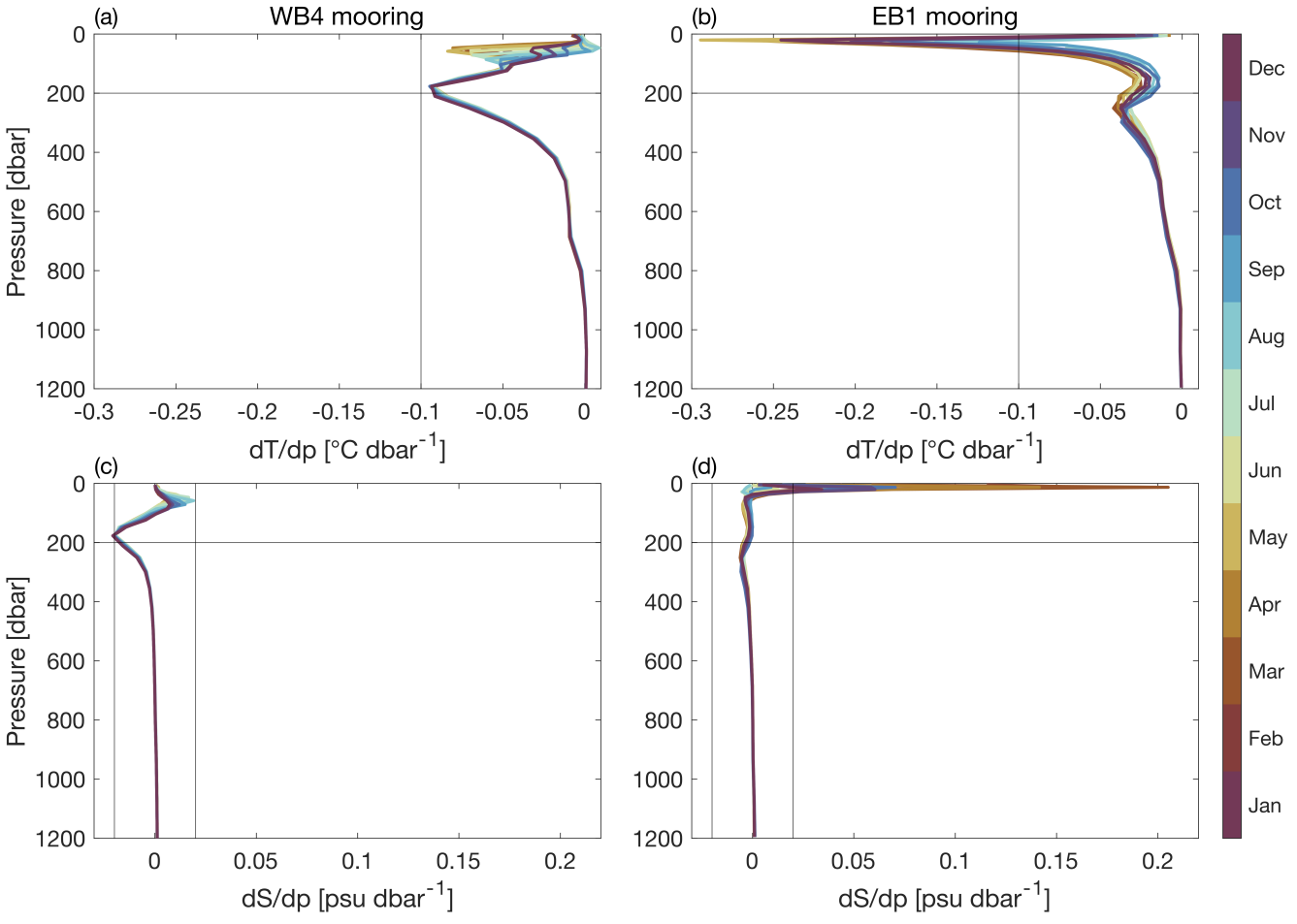

Figure C1. Monthly climatology of temperature and salinity gradients. Profiles of temperature (top) and salinity (bottom) gradients are shown for the locations of the WB4 (left) and EB1 (right) moorings. Colours indicate the months of the climatology. The black horizontal and vertical lines are supposed to aid the comparison between the WB4 and EB1 moorings.

Dealing with the absence of surface salinity measurements

We compare three different methods for the realistic case of no surface salinity measurements: 1. The surface salinity measurements are replaced by climatological surface salinity. For the gridding, this value is treated like the moored measurements. We found that a climatological seasonal cycle performs better than a single mean salinity value. The latter has been suggested at 26.5°N if an instrument is located above 100 m depth (McCarthy et al., 2015). 2. Salinity anomalies (S') are assumed constant above the uppermost instrument, that means $S'(z,t) = S'(z_{instr1},t)$ if $0\ m < z < z_{instr1}$ (Williams et al., 2015). 3. While

https://doi.org/10.5194/egusphere-2026-2983
Preprint. Discussion started: 12 June 2026

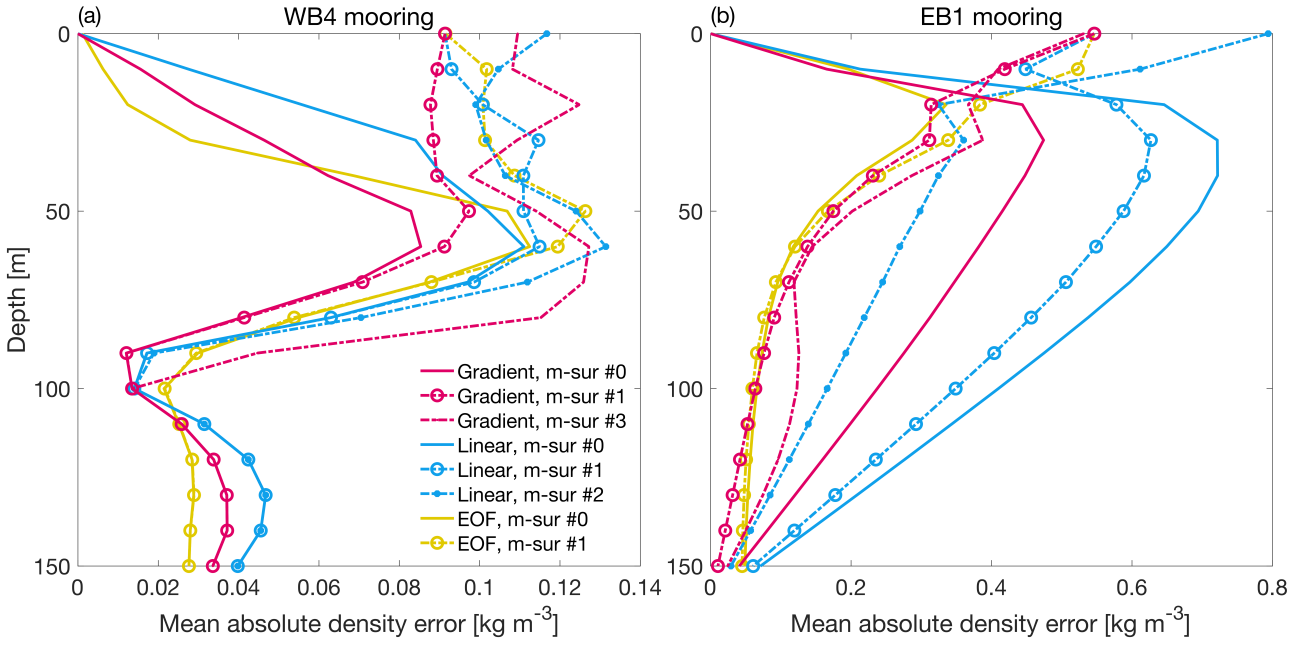

Figure C2. Time-mean absolute error of the reconstruction of density profiles for different options dealing with the absence of surface salinity measurements. Displayed are results for the WB4 (a) and EB1 (b) moorings considering for the current setup (m-wb4 #2 & m-eb1 #2) different methods to fill the vertical gaps between the instruments (stepwise integration of T&S using monthly climatological gradients (red, m-vst #1), linear interpolation of T&S anomalies (blue, m-vst #2), and EOF regression (yellow, m-vst #3)) and different methods to obtain salinity values above the uppermost instrument (idealised with surface measurement (solid, m-sur #0), replacing surface measurement by climatological surface salinity (dash-dotted line with circle, m-sur #1), constant anomaly above uppermost instrument (dash-dotted line with dot, m-sur #2), seasonal varying extrapolation (dash-dotted line without marker, m-sur #3)).

linear extrapolation towards the surface is not recommended (McCarthy et al., 2015; Williams et al., 2015), the RAPID array currently employs a seasonally varying extrapolation technique which considers besides linear also terms of higher order and found this particularly useful if the uppermost instrument is deeper than 100 m depth (McCarthy et al., 2015). Note that while McCarthy et al. (2015) use this technique to extrapolate dynamic height, here it is employed to extrapolate salinity.

Figure C2 displays the density reconstruction error in the upper 150 m for the different methods of filling the gap above the uppermost salinity measurement to the surface for the current setup. For the WB4 mooring (case with uppermost instrument above the main thermocline), the density error near the surface increases when not having a surface salinity measurement, indicating that salinity variability has an impact on density near the surface. Replacing the surface salinity measurements by a surface salinity climatology yields the smallest reconstruction errors. Both a seasonal extrapolation method and having a constant salinity anomaly above the uppermost instrument yield slightly higher density reconstruction errors. For the EB1 mooring (case with uppermost instrument below the distinct seasonal thermocline), there are two differences to the WB4 mooring re-

https://doi.org/10.5194/egusphere-2026-2983
Preprint. Discussion started: 12 June 2026

sults occurring for the depth range between the seasonal thermocline of the EB1 mooring at about 15 m to 20 m depth and the uppermost instrument at 150 m depth: 1. For linear interpolation of anomalies and EOF regression, the density error is smaller when surface salinity is not taken into account than when it is taken into account. 2. For linear interpolation of anomalies, a constant salinity anomaly above the uppermost instrument performs better than replacing the surface salinity measurements by a surface salinity climatology.

Appendix D: Reconstruction of BPRs

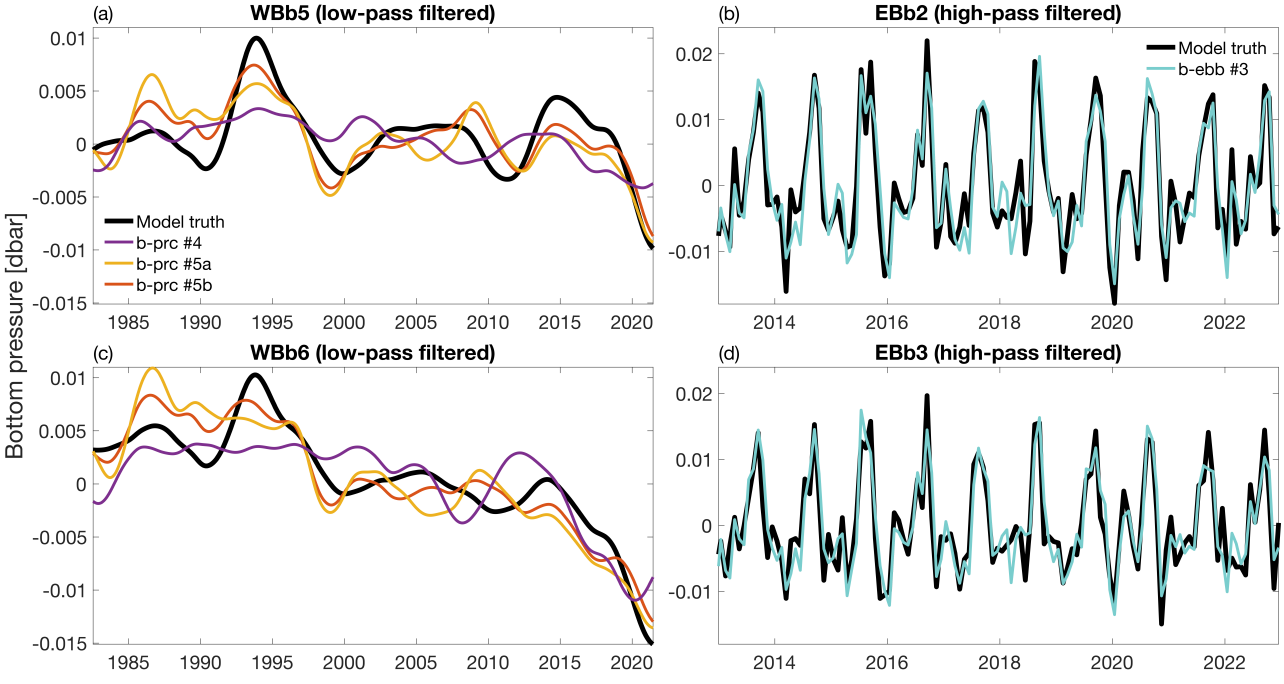

Figure D1. Reconstructed time-series of the bottom pressure for BPRs (a) WBb5, (b) EBb2, (c) WBb6, and (d) EBb3. The time series for the western boundary BPRs (a) and (c) are low-pass filtered with a 5 year cut-off and the time series for the eastern boundary BPRs (b) and (d) are high-pass filtered with a 2 year cut-off. For the latter (b) and (d), the last ten years of the time series are shown exemplary. The black line shows the model-true values. The coloured lines show different reconstructions where bottom pressure is reconstructed from acoustic travel times (b-prc # 4) and moored temperature and salinity data (b-prc #5a and #5b, and b-ebb #3). See Table 1 for further explanations.

Author contributions. ACH and PB conceptualised the work. ACH performed the analyses, produced the figures and wrote the original draft. FUS provided the model simulation. All co-authors discussed the analyses and contributed to the editing and review process.

https://doi.org/10.5194/egusphere-2026-2983
Preprint. Discussion started: 12 June 2026

Competing interests. The authors declare that they have no conflict of interest.

Disclaimer. TEXT

Acknowledgements. The authors gratefully acknowledge the Earth System Modelling Project (ESM) for funding this work by providing computing time on the ESM partition of the supercomputer JUWELS at the Jülich Supercomputing Centre (JSC). This work was also supported in part through high-performance computing resources available at the Kiel University Computing Centre. A.C. Hans was supported by Evangelisches Studienwerk Villigst. This study utilised SAFAtor, a Helmholtz Large Research Infrastructure funded by the BMFTR and coordinated by GFZ and GEOMAR. DeepL was used during the writing process for language editing and translation assistance. The authors thank Christian Mertens for helpful discussions.

https://doi.org/10.5194/egusphere-2026-2983
Preprint. Discussion started: 12 June 2026

References

Baehr, J., Hirschi, J., Beismann, J.-O., and Marotzke, J.: Monitoring the meridional overturning circulation in the North Atlantic: A model-based array design study, Journal of Marine Research, 62, 283–312, https://doi.org/10.1357/0022240041446191, 2004.

Baehr, J., Stroup, A., and Marotzke, J.: Testing concepts for continuous monitoring of the meridional overturning circulation in the South Atlantic, Ocean Modelling, 29, 147–153, https://doi.org/10.1016/j.ocemod.2009.03.005, 2009.

Barnier, B., Madec, G., Penduff, T., Molines, J.-M., Treguier, A.-M., Le Sommer, J., Beckmann, A., Biastoch, A., Böning, C., Dengg, J., Derval, C., Durand, E., Gulev, S., Remy, E., Talandier, C., Theetten, S., Maltrud, M., McClean, J., and De Cuevas, B.: Impact of partial steps and momentum advection schemes in a global ocean circulation model at eddy-permitting resolution, Ocean Dynamics, 56, 543–567, https://doi.org/10.1007/s10236-006-0082-1, 2006.

Biastoch, A., Schwarzkopf, F. U., Getzlaff, K., Rühs, S., Martin, T., Scheinert, M., Schulzki, T., Handmann, P., Hummels, R., and Böning, C. W.: Regional imprints of changes in the Atlantic Meridional Overturning Circulation in the eddy-rich ocean model VIKING20X, Ocean Science, 17, 1177–1211, https://doi.org/10.5194/os-17-1177-2021, 2021.

Bingham, R. J. and Hughes, C. W.: Determining North Atlantic meridional transport variability from pressure on the western boundary: A model investigation, Journal of Geophysical Research: Oceans, 113, 2007JC004 679, https://doi.org/10.1029/2007JC004679, 2008.

Bingham, R. J. and Hughes, C. W.: Geostrophic dynamics of meridional transport variability in the subpolar North Atlantic, Journal of Geophysical Research: Oceans, 114, 2009JC005 492, https://doi.org/10.1029/2009JC005492, 2009.

Bonan, D. B., Thompson, A. F., Schneider, T., Zanna, L., Armour, K. C., and Sun, S.: Observational constraints imply limited future Atlantic meridional overturning circulation weakening, Nature Geoscience, https://doi.org/10.1038/s41561-025-01709-0, 2025.

Buckley, M. W. and Marshall, J.: Observations, inferences, and mechanisms of the Atlantic Meridional Overturning Circulation: A review, Reviews of Geophysics, 54, 5–63, https://doi.org/10.1002/2015RG000493, 2016.

Chidichimo, M. P., Perez, R. C., Speich, S., Kersalé, M., Sprintall, J., Dong, S., Lamont, T., Sato, O. T., Chereskin, T. K., Hummels, R., and Schmid, C.: Energetic overturning flows, dynamic interocean exchanges, and ocean warming observed in the South Atlantic, Communications Earth & Environment, 4, 10, https://doi.org/10.1038/s43247-022-00644-x, 2023.

Collins, M., Sutherland, M., Bouwer, L., Cheong, S.-M., Fröhlicher, T., Jacot Des Combes, H., Koll Roxy, M., Losada, I., McInnes, K., Ratter, B., Rivera-Arriaga, E., Susanto, R., Swingedouw, D., and Tibig, L.: Extremes, Abrupt Changes and Managing Risks, Tech. rep., Cambridge University Press, Cambridge, UK and New York, NY, USA, https://doi.org/10.1017/9781009157964.008, 2019.

Crameri, F.: Scientific colour maps, https://doi.org/10.5281/ZENODO.1243862, [code], 2023.

Danabasoglu, G., Castruccio, F. S., Small, R. J., Tomas, R., Frajka-Williams, E., and Lankhorst, M.: Revisiting AMOC Transport Estimates From Observations and Models, Geophysical Research Letters, 48, e2021GL093 045, https://doi.org/10.1029/2021GL093045, 2021.

Debreu, L., Vouland, C., and Blayo, E.: AGRIF: Adaptive grid refinement in Fortran, Computers & Geosciences, 34, 8–13, https://doi.org/10.1016/j.cageo.2007.01.009, 2008.

Dong, S., Baringer, M. O., Goni, G. J., Meinen, C. S., and Garzoli, S. L.: Seasonal variations in the South Atlantic Meridional Overturning Circulation from observations and numerical models, Geophysical Research Letters, 41, 4611–4618, https://doi.org/10.1002/2014GL060428, 2014.

Dong, S., Goni, G., Domingues, R., Bringas, F., Goes, M., Christophersen, J., and Baringer, M.: Synergy of In Situ and Satellite Ocean Observations in Determining Meridional Heat Transport in the Atlantic Ocean, Journal of Geophysical Research: Oceans, 126, e2020JC017 073, https://doi.org/10.1029/2020JC017073, 2021.

https://doi.org/10.5194/egusphere-2026-2983
Preprint. Discussion started: 12 June 2026

Donohue, K. A., Watts, D. R., Tracey, K. L., Greene, A. D., and Kennelly, M.: Mapping Circulation in the Kuroshio Extension with an Array of Current and Pressure Recording Inverted Echo Sounders, Journal of Atmospheric and Oceanic Technology, 27, 507–527, https://doi.org/10.1175/2009JTECHO686.1, 2010.

Druck: RPS/DPS 8000 - High accuracy resonant pressure sensor, https://dam.bakerhughes.com/m/3f96364479f17828/original/Druck-RPS-DPS-8000-High-Accuracy-Resonant-Pressure-Sensor.pdf, 2025.

Döös, K.: Influence of the Rossby waves on the seasonal cycle in the tropical Atlantic, Journal of Geophysical Research: Oceans, 104, 29 591–29 598, https://doi.org/10.1029/1999JC900126, 1999.

Elipot, S., Frajka-Williams, E., Hughes, C. W., and Willis, J. K.: The Observed North Atlantic Meridional Overturning Circulation: Its Meridional Coherence and Ocean Bottom Pressure, Journal of Physical Oceanography, 44, 517–537, https://doi.org/10.1175/JPO-D-13-026.1, 2014.

Fillenbaum, E. R., Lee, T. N., Johns, W. E., and Zantopp, R. J.: Meridional Heat Transport Variability at 26.5°N in the North Atlantic, Journal of Physical Oceanography, 27, 153–174, https://doi.org/10.1175/1520-0485(1997)027<0153:MHTVAN>2.0.CO;2, 1997.

Fofonoff, N. P.: Dynamics of ocean currents, in: The Sea: Ideas and Observations on Progress in the Study of the Seas, vol. Physical Oceanography, pp. 323–395, Wiley-Interscience, New York, https://ia601408.us.archive.org/4/items/in.ernet.dli.2015.130422/2015.130422.The-Sea-Ideas-And-Observations-On-Progress-In-The-Study-Of-The-Seas-Vol-1.pdf, 1962.

Foukal, N., Le Bras, I., Fu, Y., Petit, T., Biló, T., Elipot, S., and Moat, B.: Strengthening Connections in Observing the North Atlantic Meridional Overturning Circulation: Outcomes from a Joint RAPID-OSNAP Workshop, Oceanography, https://doi.org/10.5670/oceanog.2026.e110, 2026.

Frajka-Williams, E., Ansorge, I. J., Baehr, J., Bryden, H. L., Chidichimo, M. P., Cunningham, S. A., Danabasoglu, G., Dong, S., Donohue, K. A., Elipot, S., Heimbach, P., Holliday, N. P., Hummels, R., Jackson, L. C., Karstensen, J., Lankhorst, M., Le Bras, I. A., Lozier, M. S., McDonagh, E. L., Meinen, C. S., Mercier, H., Moat, B. I., Perez, R. C., Piecuch, C. G., Rhein, M., Srokosz, M. A., Trenberth, K. E., Bacon, S., Forget, G., Goni, G., Kieke, D., Koelling, J., Lamont, T., McCarthy, G. D., Mertens, C., Send, U., Smeed, D. A., Speich, S., Van Den Berg, M., Volkov, D., and Wilson, C.: Atlantic Meridional Overturning Circulation: Observed Transport and Variability, Frontiers in Marine Science, 6, 260, https://doi.org/10.3389/fmars.2019.00260, 2019.

Frajka-Williams, E., Foukal, N., and Danabasoglu, G.: Should AMOC observations continue: how and why?, Philosophical Transactions of the Royal Society A: Mathematical, Physical and Engineering Sciences, 381, 20220 195, https://doi.org/10.1098/rsta.2022.0195, 2023.

Garzoli, S. L., Baringer, M. O., Dong, S., Perez, R. C., and Yao, Q.: South Atlantic meridional fluxes, Deep Sea Research Part I: Oceanographic Research Papers, 71, 21–32, https://doi.org/10.1016/j.dsr.2012.09.003, 2013.

Goldberg, M., Nguyen, A., Pillar, H., Howe, B., and Heimbach, P.: Evaluating the potential of SMART subsea cable pressure sensors to constrain Subpolar North Atlantic circulation variability through Observing System Simulation Experiments, https://doi.org/10.31223/X51F2Z, 2025.

Greatbatch, R. J.: A note on the representation of steric sea level in models that conserve volume rather than mass, Journal of Geophysical Research: Oceans, 99, 12 767–12 771, https://doi.org/10.1029/94JC00847, 1994.

Griffies, S. M. and Greatbatch, R. J.: Physical processes that impact the evolution of global mean sea level in ocean climate models, Ocean Modelling, 51, 37–72, https://doi.org/10.1016/j.ocemod.2012.04.003, 2012.

Hans, A. C., Hummels, R., Brandt, P., Schwarzkopf, F. U., and Juricke, S.: Scripts used in: "Evaluating Transport Observations of the Atlantic Meridional Overturning Circulation at 11°S Using an Ocean Model", https://doi.org/10.3289/SW_3_2026, [code], 2026.

https://doi.org/10.5194/egusphere-2026-2983
Preprint. Discussion started: 12 June 2026

Harmon, N., Rychert, C. A., Moat, B., Smeed, D., Frajka-Williams, E., Petit, T., Walker, M., Provost, P., and Thomas, T.: Implications for Oceanographic and Seafloor Geodetic Applications Due To Settling of Self-Calibrating Bottom Pressure Recorders, Geophysical Research Letters, 53, e2025GL117 927, https://doi.org/10.1029/2025GL117927, 2026.

Herrford, J., Brandt, P., Kanzow, T., Hummels, R., Araujo, M., and Durgadoo, J. V.: Seasonal variability of the Atlantic Meridional Overturning Circulation at 11°S inferred from bottom pressure measurements, Ocean Science, 17, 265–284, https://doi.org/10.5194/os-17-265-2021, 2021.

Hirschi, J., Baehr, J., Marotzke, J., Stark, J., Cunningham, S., and Beismann, J.: A monitoring design for the Atlantic meridional overturning circulation, Geophysical Research Letters, 30, 2002GL016 776, https://doi.org/10.1029/2002GL016776, 2003.

Hirschi, J. J., Barnier, B., Böning, C., Biastoch, A., Blaker, A. T., Coward, A., Danilov, S., Drijfhout, S., Getzlaff, K., Griffies, S. M., Hasumi, H., Hewitt, H., Iovino, D., Kawasaki, T., Kiss, A. E., Koldunov, N., Marzocchi, A., Mecking, J. V., Moat, B., Molines, J., Myers, P. G., Penduff, T., Roberts, M., Treguier, A., Sein, D. V., Sidorenko, D., Small, J., Spence, P., Thompson, L., Weijer, W., and Xu, X.: The Atlantic Meridional Overturning Circulation in High-Resolution Models, Journal of Geophysical Research: Oceans, 125, e2019JC015 522, https://doi.org/10.1029/2019JC015522, 2020.

Howe, B. M., Arbic, B. K., Aucan, J., Barnes, C. R., Bayliff, N., Becker, N., Butler, R., Doyle, L., Elipot, S., Johnson, G. C., Landerer, F., Lentz, S., Luther, D. S., Müller, M., Mariano, J., Panayotou, K., Rowe, C., Ota, H., Song, Y. T., Thomas, M., Thomas, P. N., Thompson, P., Tilmann, F., Weber, T., and Weinstein, S.: SMART Cables for Observing the Global Ocean: Science and Implementation, Frontiers in Marine Science, 6, 424, https://doi.org/10.3389/fmars.2019.00424, 2019.

Hughes, C. W., Elipot, S., Morales Maqueda, M. A., and Loder, J. W.: Test of a Method for Monitoring the Geostrophic Meridional Overturning Circulation Using Only Boundary Measurements, Journal of Atmospheric and Oceanic Technology, 30, 789–809, https://doi.org/10.1175/JTECH-D-12-00149.1, 2013.

Hummels, R., Brandt, P., Dengler, M., Fischer, J., Araujo, M., Veleda, D., and Durgadoo, J. V.: Interannual to decadal changes in the western boundary circulation in the Atlantic at 11°S, Geophysical Research Letters, 42, 7615–7622, https://doi.org/10.1002/2015GL065254, 2015.

Johns, W. E., Kanzow, T., and Zantopp, R.: Estimating ocean transports with dynamic height moorings: An application in the Atlantic Deep Western Boundary Current at 26°N, Deep Sea Research Part I: Oceanographic Research Papers, 52, 1542–1567, https://doi.org/10.1016/j.dsr.2005.02.002, 2005.

Johns, W. E., Speich, S., Araujo, M., and lead authors: Tropical Atlantic Observing System (TAOS) Review Report, CLIVAR-01/2021, https://horizon.documentation.ird.fr/exl-doc/pleins_textes/2024-01/010089096.pdf, 2021.

Johns, W. E., Elipot, S., Smeed, D. A., Moat, B., King, B., Volkov, D. L., and Smith, R. H.: Towards two decades of Atlantic Ocean mass and heat transports at 26.5°N, Philosophical Transactions of the Royal Society A: Mathematical, Physical and Engineering Sciences, 381, 20220 188, https://doi.org/10.1098/rsta.2022.0188, 2023.

Koelling, J., Send, U., and Lankhorst, M.: Decadal Strengthening of Interior Flow of North Atlantic Deep Water Observed by GRACE Satellites, Journal of Geophysical Research: Oceans, 125, e2020JC016 217, https://doi.org/10.1029/2020JC016217, 2020.

Kopte, R., Brandt, P., Dengler, M., Tchipalanga, P. C. M., Macuéria, M., and Ostrowski, M.: The Angola Current: Flow and hydrographic characteristics as observed at 11°S, Journal of Geophysical Research: Oceans, 122, 1177–1189, https://doi.org/10.1002/2016JC012374, 2017.

Li, F., Lozier, M. S., and Johns, W. E.: Calculating the Meridional Volume, Heat, and Freshwater Transports from an Observing System in the Subpolar North Atlantic: Observing System Simulation Experiment, Journal of Atmospheric and Oceanic Technology, 34, 1483–1500, https://doi.org/10.1175/JTECH-D-16-0247.1, 2017.

https://doi.org/10.5194/egusphere-2026-2983
Preprint. Discussion started: 12 June 2026

Lobelle, D., Beaulieu, C., Livina, V., Sévellec, F., and Frajka-Williams, E.: Detectability of an AMOC Decline in Current and Projected Climate Changes, Geophysical Research Letters, 47, e2020GL089 974, https://doi.org/10.1029/2020GL089974, 2020.

Lozier, M. S., Li, F., Bacon, S., Bahr, F., Bower, A. S., Cunningham, S. A., De Jong, M. F., De Steur, L., deYoung, B., Fischer, J., Gary, S. F., Greenan, B. J. W., Holliday, N. P., Houk, A., Houpert, L., Inall, M. E., Johns, W. E., Johnson, H. L., Johnson, C., Karstensen, J., Koman, G., Le Bras, I. A., Lin, X., Mackay, N., Marshall, D. P., Mercier, H., Oltmanns, M., Pickart, R. S., Ramsey, A. L., Rayner, D., Straneo, F., Thierry, V., Torres, D. J., Williams, R. G., Wilson, C., Yang, J., Yashayaev, I., and Zhao, J.: A sea change in our view of overturning in the subpolar North Atlantic, Science, 363, 516–521, https://doi.org/10.1126/science.aau6592, 2019.

Madec, G., Bourdallé-Badie, R., Bouttier, P.-A., Bricaud, C., Bruciaferri, D., Calvert, D., Chanut, J., Clementi, E., Coward, A., Delrosso, D., Ethé, C., Flavoni, S., Graham, T., Harle, J., Iovino, D., Lea, D., Lévy, C., Lovato, T., Martin, N., Masson, S., Mocavero, S., Paul, J., Rousset, C., Storkey, D., Storto, A., and Vancoppenolle, M.: NEMO ocean engine, Tech. Rep. v3.6-patch, Number 27, Zenodo, ISSN 1288-1619, https://doi.org/10.5281/ZENODO.3248739, version Number: v3.6-patch, 2017.

McCarthy, G., Smeed, D., Johns, W., Frajka-Williams, E., Moat, B., Rayner, D., Baringer, M., Meinen, C., Collins, J., and Bryden, H.: Measuring the Atlantic Meridional Overturning Circulation at 26°N, Progress in Oceanography, 130, 91–111, https://doi.org/10.1016/j.pocean.2014.10.006, 2015.

McCarthy, G. D., Brown, P. J., Flagg, C. N., Goni, G., Houpert, L., Hughes, C. W., Hummels, R., Inall, M., Jochumsen, K., Larsen, K. M. H., Lherminier, P., Meinen, C. S., Moat, B. I., Rayner, D., Rhein, M., Roessler, A., Schmid, C., and Smeed, D. A.: Sustainable Observations of the AMOC: Methodology and Technology, Reviews of Geophysics, 58, e2019RG000 654, https://doi.org/10.1029/2019RG000654, 2020.

McCarthy, G. D., Hug, G., Smeed, D., Morris, K. J., and Moat, B.: Signal and Noise in the Atlantic Meridional Overturning Circulation at 26°N, Geophysical Research Letters, 52, e2025GL115 055, https://doi.org/10.1029/2025GL115055, 2025.

Meinen, C. S. and Watts, D. R.: Vertical structure and transport on a transect across the North Atlantic Current near 42°N: Time series and mean, Journal of Geophysical Research: Oceans, 105, 21 869–21 891, https://doi.org/10.1029/2000JC900097, 2000.

Meinen, C. S., Speich, S., Perez, R. C., Dong, S., Piola, A. R., Garzoli, S. L., Baringer, M. O., Gladyshev, S., and Campos, E. J. D.: Temporal variability of the meridional overturning circulation at 34.5°S: Results from two pilot boundary arrays in the South Atlantic, Journal of Geophysical Research: Oceans, 118, 6461–6478, https://doi.org/10.1002/2013JC009228, 2013.

Meinen, C. S., Speich, S., Piola, A. R., Ansorge, I., Campos, E., Kersalé, M., Terre, T., Chidichimo, M. P., Lamont, T., Sato, O. T., Perez, R. C., Valla, D., Van Den Berg, M., Le Hénaff, M., Dong, S., and Garzoli, S. L.: Meridional Overturning Circulation Transport Variability at 34.5°S During 2009-2017: Baroclinic and Barotropic Flows and the Dueling Influence of the Boundaries, Geophysical Research Letters, 45, 4180–4188, https://doi.org/10.1029/2018GL077408, 2018.

Morgan, P. P. and Pender, L.: SeaWater Library of EOS-80, https://www.cmar.csiro.au/datacentre/ext_docs/seawater.html, [code], 2014.

NOAA National Geophysical Data Center: 2-minute Gridded Global Relief Data (ETOPO2) v2, https://doi.org/10.7289/V5J1012Q, 2006.

Nowitzki, H., Rhein, M., Roessler, A., Kieke, D., and Mertens, C.: Trends and Transport Variability of the Circulation in the Subpolar Eastern North Atlantic, Journal of Geophysical Research: Oceans, 126, e2020JC016 693, https://doi.org/10.1029/2020JC016693, 2021.

Paroscientific Inc.: Digiquartz Broadband Barometers, https://paroscientific.com/pdf/D40_Broadband_Barometers.pdf.

Paroscientific Inc.: Digiquartz Pressure Instrumentation, https://www.comm-tec.com/Docs/Manuali/Paros/DQAdvantage.pdf, 2011.

Perez, R. C., Garzoli, S. L., Meinen, C. S., and Matano, R. P.: Geostrophic Velocity Measurement Techniques for the Meridional Overturning Circulation and Meridional Heat Transport in the South Atlantic, Journal of Atmospheric and Oceanic Technology, 28, 1504–1521, https://doi.org/10.1175/JTECH-D-11-00058.1, 2011.

https://doi.org/10.5194/egusphere-2026-2983
Preprint. Discussion started: 12 June 2026

Petit, T., Smeed, D., Blaker, A., Elipot, S., Johns, W., Kajtar, J. B., Rayner, D., Sinha, B., Smith, R. H., Volkov, D. L., and Moat, B.: Evaluation of a Reduced RAPID Array for Measuring the AMOC, Journal of Geophysical Research: Oceans, 130, e2025JC023 093, https://doi.org/10.1029/2025JC023093, 2025.

Polster, A., Fabian, M., and Villinger, H.: Effective resolution and drift of Paroscientific pressure sensors derived from long-term seafloor measurements, Geochemistry, Geophysics, Geosystems, 10, 2009GC002 532, https://doi.org/10.1029/2009GC002532, 2009.

Rhein, M., Mertens, C., and Roessler, A.: Observed Transport Decline at 47°N, Western Atlantic, Journal of Geophysical Research: Oceans, 124, 4875–4890, https://doi.org/10.1029/2019JC014993, 2019.

Roessler, A., Rhein, M., Kieke, D., and Mertens, C.: Long-term observations of North Atlantic Current transport at the gateway between western and eastern Atlantic, Journal of Geophysical Research: Oceans, 120, 4003–4027, https://doi.org/10.1002/2014JC010662, 2015.

Rossby, T.: On monitoring depth variations of the main thermocline acoustically, Journal of Geophysical Research, 74, 5542–5546, https://doi.org/10.1029/JC074i023p05542, 1969.

Roullet, G. and Madec, G.: Salt conservation, free surface, and varying levels: A new formulation for ocean general circulation models, Journal of Geophysical Research: Oceans, 105, 23 927–23 942, https://doi.org/10.1029/2000JC900089, 2000.

Rühs, S., Getzlaff, K., Durgadoo, J. V., Biastoch, A., and Böning, C. W.: On the suitability of North Brazil Current transport estimates for monitoring basin-scale AMOC changes, Geophysical Research Letters, 42, 8072–8080, https://doi.org/10.1002/2015GL065695, 2015.

Schott, F. A., Dengler, M., Zantopp, R., Stramma, L., Fischer, J., and Brandt, P.: The Shallow and Deep Western Boundary Circulation of the South Atlantic at 5°-11°S, Journal of Physical Oceanography, 35, 2031–2053, https://doi.org/10.1175/JPO2813.1, 2005.

Shihora, L., Martin, T., Hans, A. C., Hummels, R., Schindelegger, M., and Dobslaw, H.: Relating Atlantic meridional deep-water transport to ocean bottom pressure variations as a target for satellite gravimetry missions, Ocean Science, 21, 1533–1548, https://doi.org/10.5194/os-21-1533-2025, 2025.

Sinha, B., Smeed, D., McCarthy, G., Moat, B., Josey, S., Hirschi, J.-M., Frajka-Williams, E., Blaker, A., Rayner, D., and Madec, G.: The accuracy of estimates of the overturning circulation from basin-wide mooring arrays, Progress in Oceanography, 160, 101–123, https://doi.org/10.1016/j.pocean.2017.12.001, 2018.

Stepanov, V. N., Iovino, D., Masina, S., Storto, A., and Cipollone, A.: Methods of calculation of the Atlantic meridional heat and volume transports from ocean models at 26.5°N, Journal of Geophysical Research: Oceans, 121, 1459–1475, https://doi.org/10.1002/2015JC011007, 2016.

Terhaar, J., Vogt, L., and Foukal, N. P.: Atlantic overturning inferred from air-sea heat fluxes indicates no decline since the 1960s, Nature Communications, 16, 222, https://doi.org/10.1038/s41467-024-55297-5, 2025.

Thyng, K., Greene, C., Hetland, R., Zimmerle, H., and DiMarco, S.: True Colors of Oceanography: Guidelines for Effective and Accurate Colormap Selection, Oceanography, 29, 9–13, https://doi.org/10.5670/oceanog.2016.66, [code], 2016.

Tsujino, H., Urakawa, S., Nakano, H., Small, R. J., Kim, W. M., Yeager, S. G., Danabasoglu, G., Suzuki, T., Bamber, J. L., Bentsen, M., Böning, C. W., Bozec, A., Chassignet, E. P., Curchitser, E., Boeira Dias, F., Durack, P. J., Griffies, S. M., Harada, Y., Ilicak, M., Josey, S. A., Kobayashi, C., Kobayashi, S., Komuro, Y., Large, W. G., Le Sommer, J., Marsland, S. J., Masina, S., Scheinert, M., Tomita, H., Valdivieso, M., and Yamazaki, D.: JRA-55 based surface dataset for driving ocean-sea-ice models (JRA55-do), Ocean Modelling, 130, 79–139, https://doi.org/10.1016/j.ocemod.2018.07.002, 2018.

Tuchen, F. P., Lübbecke, J. F., Brandt, P., and Fu, Y.: Observed Transport Variability of the Atlantic Subtropical Cells and Their Connection to Tropical Sea Surface Temperature Variability, Journal of Geophysical Research: Oceans, 125, e2020JC016 592, https://doi.org/10.1029/2020JC016592, 2020.

https://doi.org/10.5194/egusphere-2026-2983
Preprint. Discussion started: 12 June 2026

Tuchen, F. P., Brandt, P., Lübbecke, J. F., and Hummels, R.: Transports and Pathways of the Tropical AMOC Return Flow From Argo Data and Shipboard Velocity Measurements, Journal of Geophysical Research: Oceans, 127, e2021JC018 115, https://doi.org/10.1029/2021JC018115, 2022.

Watts, D. R. and Kontoyiannis, H.: Deep-Ocean Bottom Pressure Measurement: Drift Removal and Performance, Journal of Atmospheric and Oceanic Technology, 7, 296–306, https://doi.org/10.1175/1520-0426(1990)007<0296:DOBPMD>2.0.CO;2, 1990.

Watts, D. R., Sun, C., and Rintoul, S.: A Two-Dimensional Gravest Empirical Mode Determined from Hydrographic Observations in the Subantarctic Front, Journal of Physical Oceanography, 31, 2186–2209, https://doi.org/10.1175/1520-0485(2001)031<2186:ATDGEM>2.0.CO;2, 2001.

Weijer, W., Cheng, W., Garuba, O. A., Hu, A., and Nadiga, B. T.: CMIP6 Models Predict Significant 21st Century Decline of the Atlantic Meridional Overturning Circulation, Geophysical Research Letters, 47, e2019GL086 075, https://doi.org/10.1029/2019GL086075, 2020.

Williams, J., Hughes, C. W., and Tamisiea, M. E.: Detecting trends in bottom pressure measured using a tall mooring and altimetry, Journal of Geophysical Research: Oceans, 120, 5216–5232, https://doi.org/10.1002/2015JC010955, 2015.